

Similarity Metrics for MR Image-to-Image Translation

Melanie Dohmen^{1,*}, Mark Klemens¹, Ivo Baltruschat¹, Tuan Truong¹, and Matthias Lenga¹

¹Bayer AG, Radiology, Berlin, Germany

*melanie.dohmen@bayer.com

ABSTRACT

Image-to-image translation can create large impact in medical imaging, i.e. if images of a patient can be translated to another modality, type or sequence for better diagnosis. However, these methods must be validated by human reader studies, which are costly and restricted to small samples. Automatic evaluation of large samples to pre-evaluate and continuously improve methods before human validation is needed. In this study, we give an overview of reference and non-reference metrics for image synthesis assessment and investigate the ability of nine metrics, that need a reference (SSIM, MS-SSIM, PSNR, MSE, NMSE, MAE, LPIPS, NMI and PCC) and three non-reference metrics (BLUR, MSN, MNG) to detect 11 kinds of distortions in MR images from the BraSyn dataset. In addition we test a downstream segmentation metric and the effect of four normalization methods (Minmax, cMinMax and Zscore). Although PSNR and SSIM are frequently used to evaluate generative models for image-to-image-translation tasks in the medical domain, they show very specific shortcomings. SSIM ignores blurring but is very sensitive to intensity shifts in unnormalized MR images. PSNR is even more sensitive to different normalization methods and hardly measures the degree of distortions. Further metrics, such as LPIPS, NMI and DICE can be very useful to evaluate other similarity aspects. If the images to be compared are misaligned, most metrics are flawed. By carefully selecting and reasonably combining image similarity metrics, the training and selection of generative models for MR image synthesis can be improved. Many aspects of their output can be validated before final and costly evaluation by trained radiologists is conducted.

1 Introduction

Recent advances in generative artificial intelligence within the natural image domain have demonstrated a remarkable capability to produce synthetic images with high fidelity, capturing nuances such as lighting variations, textures, and object placements^{1,2}. These approaches typically rely on neural network architectures and the availability of large-scale datasets. One of the key techniques that have contributed to this capability are Generative Adversarial Networks (GANs)³. In GANs, a generator network learns to produce synthetic images that are then evaluated by a discriminator network, which distinguishes between real and synthetic images. Through this adversarial process, both networks iteratively improve, leading to the generation of increasingly realistic images. Other approaches for image synthesis rely on Variational Autoencoders (VAEs)^{4,5}, a class of generative models, consisting of two main components: an encoder and a decoder. The encoder network maps input images into a lower-dimensional latent space, where each point represents a latent code encoding important features of the input image. This latent representation captures the underlying structure and variability of the data. The decoder network then takes samples from the latent space and reconstructs them back into the original input space, generating synthetic images. In addition to traditional approaches like GANs and VAEs, a recent breakthrough in the field of generative deep neural networks comes from diffusion models⁶. Unlike GANs, which operate through an adversarial training scheme, diffusion models follow a different paradigm inspired by the process of diffusion in physics. These models iteratively transform a simple noise distribution into complex data distributions, such as natural images, by gradually reducing noise to the input data. Furthermore, by combining the strengths of different generative approaches, improving neural network optimization, and the increasing availability of computing resources, researchers are continuing to advance the field of synthetic image generation. The implications of these advancements are far-reaching, with applications spanning various domains such as computer vision, graphics, augmented and virtual reality, or creative arts. Still, many challenges remain, including the potential for biases in generated images, the need for improved diversity and controllability in generation, and ethical considerations surrounding the use of AI-generated content.

1.1 Image Synthesis in Medical Imaging

Researchers are now exploring the potential to transfer these results to the synthesis of medical images, where different use cases have been identified. For training deep neural networks, very large and diverse data sets are needed, but these are rarely available for medical imaging tasks. Generative networks can amend available data with synthetic samples and thereby improve the performance of other image analysis tasks⁷. Another line of research develops generative models with an additional image input as a condition. This field, referred to as image-to-image translation, aims to translate a given image to a synthetic output image, showing the same content or object as the input but with a different appearance. Input and output typically belong

to different image domains. The input domain is referred to as **source** domain, while the output belongs to a **target** domain. Depending on the availability of source and target pairs of the same patient or structure in the training data, image-to-image translation can be performed in a paired manner, also referred to as supervised. Otherwise, unpaired, also called unsupervised, image-to-image translation aims to learn how to transfer characteristics from the entire target domain to a specific input image from the source domain. These tasks are specifically interesting in medicine⁸, because they allow to translate a medical image from one domain to another. Source and target domain may differ by imaging modality or acquisition parameters, such that image-to-image translation allows translation, e.g., from computed tomography (CT) to magnetic resonance (MR) imaging, from T1-weighted MR to T2-weighted MR, or from native MR to contrast-enhanced MR. When the source image acquisition is less harmful, acquired faster, cheaper, or already existent, while the target image is preferred for diagnosis and may be more harmful, more expensive, more time-consuming, or simply not available, a large benefit for the patient is possible. For example, radiation dose, invasive or painful examinations can be reduced or even avoided. Low-quality or low-resolution images can be restored, improved, or the resolution increased⁹. For radiation therapy, which is planned based on CT images, MR to CT synthesis has been investigated.¹⁰ MR to CT synthesis is also used for facilitating registration between both modalities¹¹. The translation between different MR-sequences (T1-weighted, T2-weighted, T2-FLAIR) can complete the missing series for improved diagnosis¹². For reducing patient burden with contrast agents, researchers work on the translation of native or low-dose MR images to synthetic high contrast-enhanced images¹³.

1.2 Validation Metrics for Image Synthesis

However, validation of these approaches is not straightforward. Besides manual evaluation by humans, metrics assessing a whole distribution of synthesized images are most popular for evaluating GANs¹⁴. These metrics aim to assess the diversity of the generated images and the coverage and similarity to a reference set of images. Another group of metrics assesses the similarity between two images. In the context of image synthesis, one image is synthesized and is to be compared to a reference image, representing a desired synthesis result. A third group of metrics assesses the quality of a single image. As quality requirements may vary between tasks and image domains, metrics for different aspects have been developed, e.g., blurriness, contrast, etc.¹⁵. These metrics are referred to as quality metrics or non-reference metrics.

For paired image-to-image translation, validation can be performed on pairs of synthesized and ground truth images of the target domain. Reference metrics measure the similarity between a given synthesized target image and a reference or ground truth target image. Slight spatial misalignment between paired images remains a problem for evaluation with reference metrics, such that specialized methods have been investigated for this purpose¹⁶⁻¹⁸. In the domain of natural images, reference metrics have been extensively tested on synthetically distorted images^{19,20}. However, these results cannot be fully transferred to medical image synthesis, where the tested distortions, such as JPEG compression and transmission artifacts, are not relevant. Instead, MR imaging exhibits very specific acquisition artifacts.

1.3 Validation in the Medical Domain

Even though human assessment will remain essential for validation in the medical image domain, it is also extremely costly, as it has to be performed by domain experts. Additionally, humans assess quality subjectively and non-reproducibly. Therefore, automatic quantitative assessment with metrics is a core part of validation, where reference metrics, non-reference metrics, and evaluation of downstream tasks are most prevalent^{21,22}. Among 13 papers on image-to-image translation with generative adversarial networks (GANs) or convolutional neural networks (CNNs) in the medical domain²³, 84% use the structural similarity index measure (SSIM), and 61% use the peak signal-to-noise ratio (PSNR) for validation. A further review on synthetic contrast-enhancement of MR images²⁴ reports evaluation by SSIM and PSNR in 75% of the studies. Even though SSIM is known to underestimate blurriness²⁵ and PSNR is known to not correlate well with human perception²⁶, these shortcomings are often not appropriately accounted for. A huge amount of additional metrics has been used²³ to complement SSIM and PSNR. However, guidelines and consensus about which metrics are most appropriate for evaluating image synthesis in the medical domain seem to be missing. This validation gap is also reflected in the decreasing number of approved medical software devices with machine learning or artificial intelligence. While the number of such devices increased by 39% in 2020, the Food and Drug Administration in the United States reported an increase of only 15% and 14% in 2021 and 2022²⁷. For segmentation and classification tasks, there are already guidelines and studies to support the selection of appropriate metrics^{28,29}. By performing downstream tasks with synthesized images, such as segmentation or classification, these metrics can also be leveraged for validation of image synthesis³⁰.

1.4 Contribution

In this paper, we provide a comprehensive overview and description of 13 commonly used reference metrics that can be used for image synthesis evaluation in the medical domain (see Sec. 2). To complement validation with reference metrics, we present suitable non-reference metrics and exemplarily discuss the value of downstream task evaluation with a segmentation metric.

In the experiments in Sec. 3, we systematically assess the sensitivity of nine references and three non-reference metrics regarding 11 different distortions, that we assume to appear in MR image synthesis. Furthermore, we use three normalization methods before metric assessment and investigate their influence. Thereby, we aim to guide researchers in the appropriate selection of metrics for any desired synthesis task. Derived from the distortion experiment results in Sec. 4, we provide a set of adverse examples in Sec. 5, to showcase unexpected behaviour of the analyzed metrics. Finally, we discuss the behaviour of the metrics in the experiments in Sec. 6 and suggest recommendations for the validation of image-to-image translation methods specifically for MR image synthesis in Sec. 7.

2 Normalization and Metric Overview

In this section, we give an overview of reference and non-reference metrics for assessing the quality of images. Especially reference metrics strongly depend on intensity value ranges. Therefore, we first introduce normalization methods that are frequently used to bring MR images to a common intensity value scale.

2.1 Notation

Let I be an image with intensity $I(\mathbf{x})$ at pixel location \mathbf{x} . For two-dimensional images, let us denote $\mathbf{x} \in \mathbb{N}^w \times \mathbb{N}^h$ and $|I| = w \cdot h$ as the number of pixel locations. For three-dimensional images, $\mathbf{x} \in \mathbb{N}^w \times \mathbb{N}^h \times \mathbb{N}^d$ and $|I| = w \cdot h \cdot d$. Let I_{\max} denote the maximum intensity, I_{\min} the minimum intensity, μ_I the mean intensity, σ_I the standard deviation of all image intensities in I . A k -th percentile I_{p_k} is an intensity value, such that a fraction of $k\%$ of all pixels in I have a lower intensity.

2.2 Intensity Ranges, Data formats and Normalization Methods

Image normalization plays a crucial role in medical image processing, serving as a fundamental preprocessing step with significant implications for downstream processing, analysis, or the development algorithms. Natural images are often acquired as RGB image with an 8-bit unsigned integer data format per channel, which corresponds to a value range of (0, 255). Medical images, such as CT, MR, X-ray or ultra-sound may image exhibit much larger intensity ranges such a 12- to 16-bit unsigned integer or 32-bit floating point values. In addition, absolute intensity values may be differently scaled in qualitative imaging modalities such as MR, depending on scanner, software version or surrounding tissue. For these imaging modalities, normalization or standardization methods are needed for quantitative comparison. For metrics, that were designed for 8-bit unsigned integer data format, adaptions to the metric or normalization to the images must be considered.

Normalization or standardization is not only needed as a prerequisite for metric assessment but is usually already performed as a preprocessing step for method development. For deep-learning based methods, a reasonable and standardized scale such as (-1, 1) or (0, 1) is recommended³¹. By modality specific normalization, deep-learning based models may even improve generalizability in case of heterogeneous input data sources³². Several normalization methods are used for MR images³³, which are typically acquired in a 16-bit integer format. Z-score normalization (see sec:zscores) and clipped min-max normalization (see sec:minmax) have been applied before model training^{34,35} to achieve numerical ranges near (-1, 1) or strictly between (0, 1), respectively.

In addition, very specific normalization methods have been developed for MR (piece-wise linear histogram-matching³⁶) or even brain MR (WhiteStripe³⁷) in order to obtain quantitative comparable intensities for the same brain or body structures.

The normalization methods investigated are defined below, and an overview is shown in Tab.1.

Table 1. Overview of normalization methods. The methods with gray background are used in the experiments section. The target intensities j_{\min} and j_{\max} can be chosen arbitrarily, but are often set to [0, 1] or [-1, 1].

abbr	description	result range	references
Minmax	rescales minimum and maximum to new range	$[j_{\min}, j_{\max}]$	
cMinmax	clips at lower and upper percentiles before MinMax. More robust to high and low outliers	$[j_{\min}, j_{\max}]$	
Z-Score	Uses mean μ and standard deviation σ of an image.	$\mu_I = 0, \sigma_I = 1$	³⁸
Rescale	Fixed Range Rescaling assumes an integer data format with a fixed range, e.g. 8-bit with a range of [0,255], that is scaled to a new range	$[j_{\min}, j_{\max}]$	
PL	Piece-wise linear histogram matching, needs a training set	depends on dataset	³⁶
WS	WhiteStripe: uses mean μ_{WM} and standard deviation σ_{WM} in a white matter region of the brain	$\mu_{WM} = 0, \sigma_{WM} = 1$	³⁷

2.2.1 Z-score

Z-score normalization³³ in image processing involves applying the statistical technique of standardization to the pixel values of an image. This process ensures that the pixel intensities across the entire image follow a distribution with a mean of zero and a standard deviation of one. To perform Z-score normalization on an image, each pixel value is subtracted by the mean pixel intensity μ_I of the entire image and then divided by the standard deviation of pixel intensities σ_I . This transformation is applied to every pixel in the image independently:

$$\text{ZScore}(I) = \frac{I - \mu_I}{\sigma_I}$$

This normalization technique brings pixel intensities to a standardized scale, and hence, the relative importance of different features within an image becomes more consistent, facilitating effective comparison and downstream analysis.

2.2.2 Minmax

Minmax normalization rescales the pixel intensity values of a given image to a target intensity range of j_{\min} to j_{\max} , typically chosen as 0 and 1³⁸.

$$\text{MinMax}_{j_{\min}, j_{\max}}(I) = \frac{I - i_{\min}}{i_{\max} - i_{\min}} \cdot (j_{\max} - j_{\min}) + j_{\min}$$

Clipped MinMax normalization³⁴ is equal to MinMax normalization with previous clipping at I_{p_k} and I_{p_j} . Usually, k is selected as $100 - j$, and $j_{\min} = 0$ and $j_{\max} = 1$. This normalization is less sensitive to outliers than MinMax, but reduces the number of different intensity values and thereby removes some information.

$$\text{clip}_{I_p, I_q}(I) = \begin{cases} I_p & , \text{if } I(\mathbf{x}) \leq I_p \\ I_q & , \text{if } I(\mathbf{x}) \geq I_q \\ I(\mathbf{x}) & , \text{else} \end{cases}$$

$$\text{cMinMax}_{I_p \rightarrow j_{\min}, I_q \rightarrow j_{\max}}(I) = \text{MinMax}_{j_{\min}, j_{\max}}(\text{clip}_{I_p, I_q}(I))$$

2.2.3 Fixed Range Rescaling

When the images to be normalized are in an integer data format with a range (b_{\min}, b_{\max}) , e.g. $(0, 2^{16})$, the intensities can be rescaled to a new range (j_{\min}, j_{\max}) .

$$\text{Rescale}_{b_{\min} \rightarrow j_{\min}, b_{\max} \rightarrow j_{\max}}(I) = \frac{I - b_{\min}}{b_{\max} - b_{\min}} \cdot (j_{\max} - j_{\min}) + j_{\min} \quad (1)$$

This is especially used to convert integer data to floating-point data in a common range for neural network training³¹.

2.3 Reference Metrics

Reference metrics are based on comparing a reference image R with another image I . Both images must have the same spatial dimensions, such that $I, R \in \mathbb{N}^w \times \mathbb{N}^h (\times \mathbb{N}^d)$.

An overview of 13 proposed reference metrics is shown in Tab.2.

If the image I was not acquired with the same modality or the same time point, spatial alignment has to be ensured before applying a reference metric. For natural images, the Tampere Image Dataset¹⁹ provides data for benchmarking reference metrics compared to mean opinion scores of human readers. Many of these metrics have been used with medical images, but some modifications can become necessary for images with a data type other than 8-bit unsigned integer. In the following, we explain each reference metric and highlight important adaptions.

2.4 Structural Similarity Index Measure

The structural similarity index measure (SSIM) combines local image structure s , luminance l and contrast c . Mean, standard deviation and covariance are calculated locally for each pixel location \mathbf{x} , commonly within a d -dimensional Gaussian kernel of size 11 and $\sigma = 1.5$ and are denoted by $\mu_I(\mathbf{x})$, $\sigma_I(\mathbf{x})$, $\mu_R(\mathbf{x})$, $\sigma_R(\mathbf{x})$ and $\sigma_{I,R}(\mathbf{x})$ respectively.

Table 2. Overview of reference and non-reference metrics. The dark highlighted methods are analyzed in the experiments section.

	abbr	description	low → high sim.	implementation	ref.
SSIM	SSIM	structural similarity index measure: combination of structure, luminance and contrast	0 ↗ 1	torchmetrics ³⁹ , scikit-image ⁴⁰	41
	MS-SSIM	Multi-Scale SSIM: SSIM on original and 4 downsampled image resolutions	0 ↗ 1	torchmetrics ³⁹	42
	CW-SSIM	Complex Wavelet SSIM ignores phase shifts in the wavelet domain, ignore small rotations and spatial translations	0 ↗ 1	gitHub ⁴³	16
PSNR	PSNR	peak signal-to-noise-ratio: relation of data range to MSE	0 ↗ ∞	torchmetrics ³⁹ , scikit-image ⁴⁰	44
	NMSE	normalized mean squared error	∞ ↘ 0		
Learned Metrics	MSE	mean squared error	∞ ↘ 0	scikit-learn ⁴⁵	
	MAE	mean absolute error	∞ ↘ 0	scikit-learn ⁴⁵	
	LPIPS	Learned perceptual image patch similarity	0 ↗ 1	pypi ⁴⁶ , torchmetrics ³⁹	47
	DISTS	Deep Image Structure and Texture Similarity Metric	0 ↗ 1	gitHub ^{43,48}	18
Statistical Dependence	MI	mutual information: correlation of bin contents	0 ↗ ∞	itk ⁴⁹	50
	NMI	normalized mutual information: MI with fixed range	1 ↗ 2	scikit-image ⁴⁰	
	PCC	Pearson Correlation Coefficient	0 ↗ 1	scikit-learn ⁴⁵	
	DICE	segmentation metric on downstream segmentation task	0 ↗ 1	itk ⁴⁹	
Non-Reference Metrics	BLUR	Blurriness by difference to additionally blurred image version		scikit-image ⁴⁰	51
	BLUR2	Blurriness by edge detection in additionally blurred image version			52
	MSN	Mean structural noise: mean correlation between neighbored rows and columns	-		53
	MNG	Mean nyquist ghosting: mean correlation between rows and columns, that are with half image distance apart	-		53

$$\text{local-SSIM}(I, R, \mathbf{x}) = \underbrace{\left(\frac{\sigma_{I,R}(\mathbf{x}) + C_3}{\sigma_I(\mathbf{x})\sigma_R(\mathbf{x}) + C_3} \right)^\alpha}_{\text{structure}} \cdot \underbrace{\left(\frac{2\mu_I(\mathbf{x})\mu_R(\mathbf{x}) + C_1}{\mu_I(\mathbf{x})^2 + \mu_R(\mathbf{x})^2 + C_1} \right)^\beta}_{\text{luminance}} \cdot \underbrace{\left(\frac{2\sigma_I(\mathbf{x})\sigma_R(\mathbf{x}) + C_2}{\sigma_I(\mathbf{x})^2 + \sigma_R(\mathbf{x})^2 + C_2} \right)^\gamma}_{\text{contrast}} \quad (2)$$

The local-SSIM is then averaged for all pixel locations \mathbf{x} . Commonly, structure, luminance and contrast are weighted equally with $\alpha = \beta = \gamma$ and the constant parameters are reduced with $C_3 = C_2/2$.

$$\text{SSIM}(I, R) = \frac{1}{|I|} \sum_{\mathbf{x} \in R} \frac{(2\mu_I(\mathbf{x})\mu_R(\mathbf{x}) + C_1) \cdot (2\sigma_{I,R}(\mathbf{x}) + C_2)}{(\mu_I(\mathbf{x})^2 + \mu_R(\mathbf{x})^2 + C_1) + (\sigma_I(\mathbf{x})^2 + \sigma_R(\mathbf{x})^2 + C_2)} \quad (3)$$

The other constants are commonly selected as $C_1 = (0.01 \cdot L)^2$, $C_2 = (0.03 \cdot L)^2$, with L defined as the data range⁴¹.

SSIM is 1.0 for identical images and decreases with lower similarity down to 0.

Several variants of SSIM exist. Multi-scale SSIM (MS-SSIM)⁴² is more sensitive towards differences in full resolution images and compares, which can be undesired for synthesis of high resolution images.

Complex-wavelet SSIM (cw-SSIM)¹⁶ was specifically designed to compensate for small rotations and spatial translations. As a drawback of ignoring phase shifts in the wavelet domain, artificial phase shifts could be introduced, when cw-SSIM is used for model optimization⁵⁴.

SSIM was developed for natural images with an 8-bit unsigned integer format and the data range parameter L is then set to 255. For non-normalized MR images with a 16-bit range, $L = 2^{16}$ could be used, however the non-quantitative MR acquisition should rather be normalized to a floating point value range before metric assessment. The correct choice of parameter L or parameters C_1 , C_2 and C_3 in case of floating point data is still being discussed. While data dependent choices of the constants are proposed as well as prior normalization by quantiles⁵⁵, current implementations assume a fixed range of (-1,1) and thereby set $L = 2^{40}$ for all floating point valued images or suggest to use the actual value range $L = (I_{\min}, I_{\max})$ ³⁹ as data range.

When the data range parameter L is chosen too large, the three components of SSIM are dominated by the constants C_1 , C_2 and C_3 and SSIM produces values that are too high. If the data range parameter is chosen too low, SSIM may underestimate similarity.

The choice for the data range L parameter is directly related to previous image normalization by rescaling (see 2.2.3). If images I and R are rescaled from an assumed value range of $B = b_{\max} - b_{\min}$ to range (0,1), then calculating SSIM with $L = 1$ on these rescaled images is the same as calculating SSIM on the unscaled images with $L = B$.

We propose to set L to the actual intensity range and additionally ensure symmetry between I and R : with $L = \max(I_{\max}, R_{\max}) - \min(I_{\min}, R_{\min})$. Applying different normalization methods, should have a similar effect as different choices of the data range parameter L .

2.5 Peak signal-to-noise ratio

Peak signal-to-noise ratio (PSNR) was developed to measure the reconstruction quality of a lossy compressed image compared to the uncompressed reference image⁴⁴. However, it is frequently used as a similarity metric, where the maximum PSNR can be infinite for identical images and 0 for completely different images. The peak signal L is analogous to the data range parameter in SSIM and is then divided by the noise, which is measured as the mean square error (MSE, see 2.6).

$$\text{PSNR}(I, R) = 10 \cdot \log_{10} \left(\frac{L^2}{\text{MSE}(I, R)} \right) = 20 \cdot \log_{10}(L - 10) \cdot \log_{10}(\text{MSE}(I, R)) \quad (4)$$

As in SSIM, the data range L has to be chosen with care. By above formula, $\log(L - 10)$ directly scales the PSNR value.

For natural images, improved variants of PSNR called PSNR-HVS and PSNR-HVS-M, that seem to correlate closer to the human visual system¹⁹, have been developed.

2.6 Error Metrics

This group of metrics, including mean absolute error (MAE), mean square error (MSE), root mean square error (RMSE) and normalized mean square error (NMSE), directly depends on the error $R(\mathbf{x}) - I(\mathbf{x})$ at each pixel location \mathbf{x} . σ_R denotes the corrected sample standard deviation of image R .

$$\begin{aligned} \text{MAE}(I, R) &= \frac{1}{|I|} \sum_{\mathbf{x}} |R(\mathbf{x}) - I(\mathbf{x})| \\ \text{MSE}(I, R) &= \frac{1}{|I|} \sum_{\mathbf{x}} (R(\mathbf{x}) - I(\mathbf{x}))^2 \\ \text{RMSE}(I, R) &= \sqrt{\frac{1}{|I|} \sum_{\mathbf{x}} (R(\mathbf{x}) - I(\mathbf{x}))^2} \\ \text{NMSE}(I, R) &= \frac{1}{|I| \cdot \sigma_R} \cdot \sum_{\mathbf{x}} (R(\mathbf{x}) - I(\mathbf{x}))^2 \end{aligned}$$

MSE, RMSE, and NMSE give more weight to large differences than MAE. By normalization with σ_R , NMSE allows images with a broadly distributed intensity range to deviate more than images with a very narrow intensity range. However, all these metrics strongly depend on the intensity values and thereby also on the normalization method.

2.7 Learned Metrics

Learned perceptual image patch similarity (LPIPS) uses a trained image classification model to extract and compare image features between a given image and a reference. Typically, an Alex-Net or VGG-architecture trained on ImageNet is employed⁴⁷. Even though it was trained on RGB images, the input images are rescaled to $[-1, 1]$ by minmax normalization for training. Therefore, images with other intensity value ranges should be similarly rescaled. LPIPS has shown great correlation with human perception and outperforms many other similarity metrics on natural images⁴⁷. Different weights and networks are possible. We analyzed LPIPS with Alex-Net as a feature extractor in Sec. 3. Although, to our knowledge, it has not been used for validation of medical image synthesis, it is commonly used as perceptual loss for training medical image-to-image translation models²².

The Deep Image Structure and Texture Similarity (DISTS) metric is an adaption of LPIPS giving more focus on texture with less sensitivity to local displacement. For example, max-pooling is replaced by $m_{\downarrow 2}$ pooling, euclidean feature distance measurement is replaced by local and global SSIM feature distance measurement and an additional loss E_2 was used for training, that was itself trained to reconstruct textures with small spatial distortions¹⁸.

2.8 Statistical Dependency Metrics

Mutual information (MI) and normalized mutual information (NMI) estimate the amount of information of an image R , that can be predicted from image I .

MI is widely used for multi-modal image registration, and it was shown, that it correlates to the degree of spatial transforms⁵⁰. It has been used sporadically as a metric for image synthesis^{23,33}.

The entropy $H(I)$ is defined with $p_I(\mathbf{x})$ as the probability, that intensity $I(\mathbf{x})$ appears in image I . The joint entropy $H(I, R)$ is defined with probability $p_{I,R}(\mathbf{x})$, that intensity $I(\mathbf{x})$ appears in I and $R(\mathbf{x})$ appears in image R at the same pixel location \mathbf{x} .

$$\begin{aligned} H(I) &= - \sum_{\mathbf{x} \in I} p_I(\mathbf{x}) \log p_I(\mathbf{x}) & MI(I, R) &= H(I) + H(R) - H(I, R) \\ H(I, R) &= - \sum_{\mathbf{x} \in I} \sum_{\mathbf{y} \in R} p_{I,R}(\mathbf{x} \in I, \mathbf{y} \in R) \log p_{I,R}(\mathbf{x}, \mathbf{y}) & NMI(I, R) &= \frac{H(I) + H(R)}{H(I, R)} \end{aligned}$$

While MI ranges between 0 and infinity, NMI has a range of $[1, 2]$, which is preferable for comparing absolute metric scores and interpretability.

Mutual information is related to the Pearson correlation coefficient (PCC), which measures the degree of a strictly linear dependency between the intensities in $I(\mathbf{x})$ and $R(\mathbf{x})$ at each pixel location \mathbf{x} . in case of perfect linear correlation, PCC is 1 and NMI is 2 (for a sufficient number of bins). For a mean intensity μ_I of image I , and μ_R of image R , PCC is defined as:

$$PCC(R, I) = \frac{\sum_{\mathbf{x} \in I, R} (R(\mathbf{x}) - \mu_R)(I(\mathbf{x}) - \mu_I)}{\sqrt{\sum_{\mathbf{x} \in I} (I(\mathbf{x}) - \mu_I)^2} \sqrt{\sum_{\mathbf{x} \in R} (R(\mathbf{x}) - \mu_R)^2}}$$

The PCC may indicate very low similarity if the relation between pixel values in image I and R is non-linear and is thereby more strict than MI. By definition, the statistical dependency metrics introduced here are insensitive to any normalization methods that apply (piece-wise) linear scaling.

2.9 Indirect Evaluation with Downstream Tasks

Medical image-to-image translation is most often performed in order to improve medical diagnosis or treatment. In this context, synthetic images must be interpreted in the same way as the reference image, but deviations, that are meaningless for interpretation can be accepted.

As an example, if a synthetic MR image is generated for detecting a brain tumor, it is irrelevant if healthy brain tissue in the synthetic image is brighter or slightly differently structured than in the true reference image, as long as it is clearly identified as healthy tissue. If a synthetic histology image is rated with the same grade of cancer as the reference image, the exact cell-wise correspondence might not be important.

Many downstream tasks can be performed automatically and can include

- Detection or segmentation of organs, cells and lesions
- Classification of images or image segments
- Transfer learning and data augmentation
- Multi-modal registration
- Dose calculation in radiation therapy planning

Detection, Segmentation and classification metrics for the biomedical domain have been well documented and discussed^{28,29}.

Therefore, the performance of such tasks with synthetic images can be well compared to the performance with reference images to validate the use of synthetic images for a specific task. The concept of downstream task evaluation metrics recognizes that the final goal of image synthesis in the medical domain is to generate useful and correct images rather than images, that are visually appealing.

However, if the images are visually presented to medical practitioners or used for other non-related objectives, successful downstream task evaluation can be quite misleading. Furthermore, the evaluation of downstream tasks can substantially depend on the performance of the downstream task method. If a segmentation model fails on a large set of the reference images, the comparison to segmentations on the synthetic images is obsolete.

The amount and variety of downstream tasks and corresponding metrics is almost unlimited, but to discuss and analyze the value of downstream tasks, we include the evaluation of a downstream segmentation model with a popular segmentation metric, namely the DICE score^{28,56}. For segmentations S_I and S_R of images I and R respectively, the DICE score relates the intersection of both segmentations to the sum of their sizes.

$$\text{DICE}(S_I, S_R) = 2 \frac{S_I \cap S_R + \epsilon}{|S_I| + |S_R| + \epsilon}$$

In the best case of identical segmentations the DICE is 1. If only one of the segmentations is empty, the DICE is 0. A very small $\epsilon > 0$ assures, that the DICE is not undefined, when both segmentations are empty, but instead also becomes 1.

2.10 Non-Reference Quality Metrics

Non-reference metrics, often also called quality metrics or blind metrics, try to assess the quality of a distorted image without knowing the undistorted reference. As a reference might not be available, these metrics can be applied in many evaluation settings. However, there is a huge amount of such metrics and most of them assume a certain kind of distortion to be detected. The correlation of many of these metrics with human perception has been investigated¹⁵. Blurriness metrics were quite successful in detecting images with reduced quality as perceived by humans in different image domains.

In this paper, we select and present only a very small set of quality metrics (see Tab. 2), that could possibly complement reference metrics and detect especially those distortions, that are missed by (some) reference metrics. It has often been discussed^{57,58}, that error metrics are not sensitive to blurring, and that synthesis models typically struggle with blurry results. That is why we specifically present blurriness metrics, that do not need a reference. In addition, we would like to assess metrics, that detect MR typical distortions, such as ghosting or stripe artifacts⁵³.

2.10.1 Blurriness Metrics

Several metrics have been investigated to measure the sharpness or, inversely, the blurriness of images to filter out low-quality images¹⁵.

For each dimension d , BLUR⁵¹ creates a blurred version \tilde{I} of image I by convolution with a uniform kernel $U_{k,d}$ of size k along d . The differences of neighboring pixels along d are summed up for \tilde{I} and I to \tilde{D} and D respectively. Then the sum of positive differences between \tilde{D} and D is related to the sum of differences D only as a measure of blurriness. BLUR is

implemented in the scikit-image python library⁴⁰ with a default of $k = 11$. The vertical measures D_v , V_h and S_h are calculated analogously to the horizontal measures D_h , V_h and S_h :

$$\begin{aligned}\tilde{I} &= \text{Conv}(U_{k,d}, I) \\ D_h(x, y) &= |I(x, y) - I(x, y+1)| \quad V_h = \sum_{x=0}^{s_x-1} \sum_{y=0}^{s_y-1} \max(0, D_h(x, y) - D(x, y+1)) \\ \tilde{D}_h(x, y) &= |\tilde{I}(x, y) - I(x, y)| \quad S_h = \sum_{x, y} D_h(x, y) \\ \text{BLUR} &= \max_{d \in \{h, v\}} \frac{S_d - V_d}{S_d}\end{aligned}$$

In summary, the difference between an image and its blurred version is compared. If there is a large difference, it is assumed, that it was not very blurry. If the difference is low, it is assumed, that it was a blurry image.

A second blur metric⁵² is the ratio of blurred edges B and non-blurred edges E . The calculation for vertical measures D_v , \tilde{D}_v , C_v , E_v and R_v is similar to the horizontal measures D_h , \tilde{D}_h , C_h , E_h and R_h .

$$\begin{aligned}D_h(x, y) &= |I(x, y-1) - I(x, y+1)| & \tilde{D}_h &= \frac{1}{s_x + s_y} \sum_x \sum_y D_h(x, y) \\ C_h(x, y) &= \begin{cases} D_h(x, y) & \text{if } D_h(x, y) > \tilde{D}_h \\ 0 & \text{otherwise} \end{cases} & E_h(x, y) &= \begin{cases} 1 & \text{, if } C_h(x, y) > C_h(x, y-1)C_h(x, y+1), \\ 0 & \text{otherwise} \end{cases} \\ R_h(x, y) &= \frac{2|I(x, y) - D_h(x, y)|}{D_h(x, y)} & B(x, y) &= \begin{cases} 1 & \text{, if } \max(R_h(x, y), R_v(x, y)) > 0.1 \\ 0 & \text{otherwise} \end{cases} \\ \text{BLUR2} &= \frac{\sum_{x, y} B(x, y)}{\sum_{x, y} E(x, y)}\end{aligned}$$

This metric also creates a blurry version from the original image to be assessed for blurriness. BLUR2 specifically detects edges in both versions with a fixed threshold and then compares how much the number of detected edge pixels decreased. In blurry images there is only a small number of edges, that might not be removed by further blurring. In very sharp images, many edges can be detected, and will vanish with blurring.

2.10.2 MR Quality Metrics

In MR images, specific artifacts may appear, which are related to image acquisition and reconstruction. These artifacts may not only appear on real images, but could be reproduced in synthetic images, which is undesirable. Therefore, the use of MR specific quality metrics could efficiently improve validation of MR synthesis models.

In order to select the preferred image from a repeated set of image acquisitions of the same patient, Schuppert et al.⁵³, evaluated a set of image quality metrics. Mean structural noise (MSN) and mean nyquist-ghosting (MNG) were revealed to best correlate with the selected image, that was perceived to have the best quality.

The mean structural noise (MSN) is the mean correlation between neighboring lines of pixels in an image, where $I_r(x)$ is the x^{th} row and $I_c(y)$ is the y^{th} column in I .

$$\text{MSN} = \frac{1}{s_x - 1} \sum_{x=0}^{s_x} \text{Corr}(I_r(x), I_r(x+1)) + \frac{1}{s_y - 1} \sum_{y=0}^{s_y} \text{Corr}(I_c(y), I_c(y+1))$$

The mean Nyquist ghosting (MNG) is the mean correlation between image lines, that are separated by $\frac{s_x}{2}$ or $\frac{s_y}{2}$ respectively.

$$\text{MNG} = \frac{2}{s_x} \sum_{x=0}^{\frac{s_x}{2}} \text{Corr}\left(I_r(x), I_r\left(x + \frac{s_x}{2}\right)\right) + \frac{2}{s_y} \sum_{y=0}^{\frac{s_y}{2}} \text{Corr}\left(I_c(y), I_c\left(y + \frac{s_y}{2}\right)\right)$$

It was assumed, that these metrics are able to detect MR specific quality issues, such as motion and ghosting artifacts.

3 Experiments

In order to systematically investigate reference and non-reference metrics, we distorted 100 MR images with 11 different types of distortions in five strengths. For the reference metrics (see Sec. 2.3), the similarity between each distorted image and its undistorted reference was calculated. For the non-reference metrics (see Sec. 2.10), the metric scores for all distorted and undistorted images were assessed. For the segmentation metric (see Sec. 2.9), we trained a model and predicted segmentations for all distorted and undistorted images. The segmentation metric assessed the agreement between segmentations derived from undistorted images and segmentations derived from the respective undistorted reference image. In addition, images were left with raw intensity values or individually normalized with one of four different normalization methods.

In image-to-image tasks, MR input or target images are typically normalized for model training and the synthesized images are generated in this normalized space. Validation of synthesized images can either be performed in this normalized space, such that the normalized target image is used as reference and the synthesized image is assumed to already be normalized appropriately. Another possibility is to invert the previously performed normalization method on the synthesized image to a non-normalized intensity range. Then the synthesized image can be compared to the target image in the original intensity range. Applying or not applying normalization to the distorted images and the undistorted reference, should simulate these options.

The LPIPS metric requires an input range of [-1 and 1]. When conducting experiments with different normalization methods, we decided to apply MinMax or cMinMax normalization to a target range of [-1, 1] instead of the default range [0, 1]. After histogram equalization, we additionally applied MinMax normalization to [-1, 1]. The experiments without normalization were actually performed with previous ZScore normalization to achieve a range close to [-1, 1]. Input images with raw intensity range were not expected to lead to reasonable results.

In the following, details of the data, the segmentation model and the distortions are given.

3.1 Data

The data was taken from the BraSyn 2023 challenge⁵⁹ training set, which consists of 1251 T1-weighted (T1n), T1-weighted contrast-enhanced (T1c), T2-weighted (T2w), T2-weighted FLAIR (T2f) and tumor segmentation masks of three classes (whole tumor, tumor core, enhancing tumor). We selected the first 100 cases of the T1c training set images as reference images. For better visualization and reduced computation time, we extracted the centered 2D slice of each 3D volume.

3.2 Segmentation model for downstream task

We trained an automatically configuring U-Net based segmentation network⁶⁰ on the T1c images of the BraSyn dataset to perform a segmentation task with three classes (1: whole tumor, 2: tumor core, 3: enhancing tumor).

The architecture of the U-Net included five residual blocks, with downsampling factors 1, 2, 2, 4 and 4, initially 32 features and one output channel activated by a sigmoid function per class. Although the segmentation masks of the BraSyn data originally consist of 4 classes (3 tumor classes and background), the model was trained with 3 output channels, assuming that a class was present, when the respective output channel exceeded a threshold of 0.5, and when all higher indexed classes were not preset. As a preprocessing step for training and inference, zscore normalization was applied to the input images. Therefore, no other normalization methods were tested.

The segmentations were evaluated with the DICE score 2.9 for the foreground (class ≥ 1) and for each class individually.

3.3 Distortions

We selected a wide range of distortions, which we expect to appear with MR image synthesis. The parameters of all distortions were scaled to 5 increasing strengths, where a strength of 1 should be a minimal distortion, which is not immediately visible and 5 a strongly visible distortion, which clearly impedes any diagnosis. We initially scaled the distortion parameters to comparable strengths by a reader study with 6 experienced researchers. The final parameters for each distortion and distorted example images are listed in Tabs. 3 and 4.

Among the selected distortions, translation and elastic deformation were applied as spatial transforms, that are commonly found, when the reference is not well aligned to the image to be tested. This is frequently the case in image-to-image translation, when the input image was acquired with a different modality or at a different time point. Usually, the patient has moved in between and registration was possibly not sufficient. Translation was modeled as an equal shift of all pixels along the x and y-axis. Elastic deformation was modeled by placing a grid with a decreasing number of points on the image, randomly displacing grid points, and linearly interpolating between the new point positions.

Intensity distortions, that shift, stretch or compress the histogram, such as gamma transforms or an intensity shift, can appear between different scanning parameters, because MR does not guarantee a fixed intensity scale. For gamma transforms, images are first normalized by MinMax to range (0, 1). This ensures, that the intensity value range is unchanged under gamma transformation. Then, the intensities are scaled back to the original intensity range. Intensity shifts are modeled by adding a fixed value to the intensity value of all pixels.

Further distortions, that represent typical acquisition artifacts of MR images are ghosting, stripe and bias field artifacts. Ghosting artifacts appear as shifted copies of the image, arising from erroneous sampling in the frequency space. Single pixel artifacts in the frequency space cause artificial stripes. Bias fields appear as low frequency background signals, that we model by multiplying with an exponential of a polynomial function of degree three (see Fig. 1). All of these distortions may moderately expand the intensity range of the distorted image compared to the reference image.

Gaussian noise or Gaussian blurring are not restricted to MR acquisition but, as in most imaging modalities, frequently observed.

Last, we investigate the effect of replace artifacts, where parts of the image content are replaced, in this case by mirrored regions. In the BraSyn data set, in most cases, there is a tumor in exactly one hemisphere of the brain. Mirroring up to the centered sagittal plane, a second tumor is inserted into, or a tumor is removed from the second hemisphere. The generation of synthetic structures, that were learned in the training set, but are not present in the respective reference image, is a known problem of cycleGAN architectures⁶¹. The detection of such synthetically inserted artifact structures is highly desired for image-to-image translation model validation.

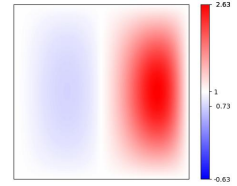


Figure 1. Bias Field

Table 3. Distortions based on spatial and intensity transforms. Parameters are given for strengths $s = 1$ and $s = 5$. All other strengths are interpolated linearly between the given values. Calculation of distorted image \tilde{I} . Let $\mathbf{s} = (w, h)$ be the image size vector of I and $T_{\mathbf{t}}(I)$ the translation of image I by vector \mathbf{t} . The minimum and maximum intensity are denoted by I_{\min}, I_{\max} .

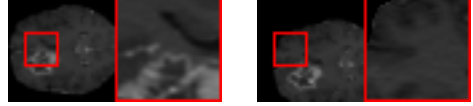
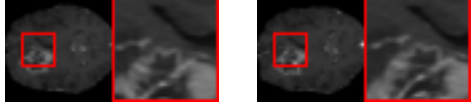
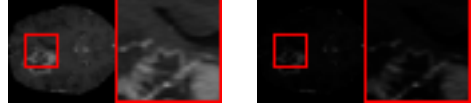
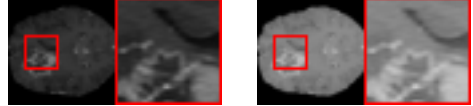
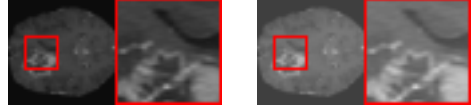
Distortion	parameter $s = 1 \rightarrow s = 5$	calculation	example images	
			$s = 1$	$s = 5$
Spatial	Translation	fraction f $0.01 \rightarrow 0.2$	$\tilde{I} = T_{f \cdot (w, h)}(I)$	
	Elastic Deform	points n $18 \rightarrow 11$ displ. d $0.03 \rightarrow 0.1$	Create a grid with n^2 points, displace points by $\mathcal{N}(\mu = 0; \sigma = d \cdot \frac{s}{n})$	
Intensity	Gamma High	$\log(\gamma)$ $0.095 \rightarrow 0.916$	$\tilde{I} = \text{MinMax}^{-1}(\text{MinMax}(I)^\gamma)$	
	Gamma Low	$\log(\gamma)$ $-0.01 \rightarrow (-0.916)$	$\tilde{I} = \text{MinMax}^{-1}(\text{MinMax}(I)^\gamma)$	
Shift Intensity	fraction f $0.05 \rightarrow 0.25$	$\tilde{I} = I + f \cdot I_{\max}$		

Table 4. Other general image distortions and MR acquisition specific artifacts. Parameters are given for strengths $s = 1$ and $s = 5$. All other strengths are interpolated linearly between the given values. Calculation of distorted image \tilde{I} . Let $\mathbf{s} = (w, h)$ be the image size vector of I . The maximum intensity of image I is denoted by I_{\max} . The fast Fourier transform is $FFT(I)$, $shift(I)$ moves frequency 0 to the center.

Distortion	parameter $s = 1 \rightarrow s = 5$	calculation	example $s = 1$	images $s = 5$
MR Acquisition Artifacts	Bias Field	coefficient c $0.5 \rightarrow 10$ $\mathcal{P}_3: \text{polynomial function of order 3}$ $BF = c \cdot \mathcal{P}_3$ $\tilde{I} = I \cdot e^{BF}$		
	Ghosting	intensity i $0.05 \rightarrow 0.4$ $I' = shift(FFT(I))$ partially distort spectrum: $I''(x \% 2 = 0) = I' \cdot i$ $I''(x = w/2) = I'$ $\tilde{I} = shift^{-1}(FFT^{-1}(I''))$		
	Stripe Artifact	intensity i $0.05 \rightarrow 0.3$ $I' = FFT(shift(I))$ $I'(0.3 \cdot \pi, 0) = i$ I'_{\max} $\tilde{I} = FFT^{-1}(shift^{-1}(I'))$		
Other Distortions	Gaussian Blur	σ $0.2 \rightarrow 1.3$ $\tilde{I} = Conv(G_{\sigma}, I)$ where G_{σ} is a Gaussian kernel		
	Gaussian Noise	σ $0.005 \rightarrow 0.05$ $\tilde{I} = I + \mathcal{N}(\mu = 0; \sigma)$		
	Replace Artifact	fraction f $0.1 \rightarrow 1.0$ $\tilde{I}(x, y) = \begin{cases} I(x, y) & , \text{if } y \leq \frac{h}{2} \\ I(x, h - y) & , \text{if } y > \frac{h}{2} \end{cases}$		

Table 5. Metric results without normalization. The darker the background the more sensitive the metric to this distortion.

metric low→high	SSIM 0→1	PSNR 0→∞	MSE 0→∞	NMSE ∞→0	MAE 0→∞	LPIPS 1→0	NMI 1→2	PCC 0→1	DICE 0→1
Distortions									
Bias Field	0.90	23.96	2736398.93	2209.31	591.53	0.15	1.28	0.77	0.59
Ghosting	0.88	37.44	18141.66	14.54	70.71	0.09	1.37	0.99	0.78
Stripe Artifact	0.27	28.14	125384.27	100.54	211.57	0.53	1.36	0.96	0.31
Gaussian Blur	0.94	33.94	39212.59	31.10	54.04	0.25	1.41	0.99	0.41
Gaussian Noise	0.39	27.92	202141.36	163.49	326.09	0.82	1.16	0.93	0.36
Replace Artifact	0.90	27.59	169258.24	136.24	95.73	0.09	1.40	0.94	0.52
Gamma High	0.75	18.40	1244788.63	996.45	548.52	0.18	1.61	0.80	0.54
Gamma Low	0.89	15.38	3352339.04	2662.40	891.89	0.09	1.80	0.98	0.60
Shift Intensity	0.25	13.98	6681345.98	5331.05	2268.45	0.00	2.00	1.00	1.00
Translation	0.65	18.28	1194718.90	963.96	503.14	0.44	1.07	0.53	0.32
Elastic Deform	0.87	28.10	145465.80	115.90	98.88	0.09	1.32	0.95	0.76

4 Results

4.1 Reference Metrics

The results for all strengths are given in Figs. A.1-A.4. In Tab. 5 - 8, the results for distortions of maximal strength (s=5) are summarized.

Table 6. Metric results with Minmax normalization. The darker the background the more sensitive the metric to this distortion.

metric low→high	SSIM 0→1	PSNR 0→∞	MSE 0→∞	NMSE ∞→0	MAE 0→∞	LPIPS 1→0	NMI 1→2	PCC 0→1
Distortions								
Bias Field	0.86	20.97	0.01	0.07	0.05	0.17	1.28	0.77
Ghosting	0.31	21.18	0.01	0.07	0.09	0.07	1.37	0.99
Stripe Artifact	0.27	28.12	0.00	0.01	0.03	0.30	1.36	0.96
Gaussian Blur	0.93	25.68	0.01	0.04	0.03	0.19	1.41	0.99
Gaussian Noise	0.17	15.95	0.03	0.20	0.16	0.65	1.16	0.93
Replace Artifact	0.89	26.79	0.00	0.02	0.02	0.07	1.40	0.94
Gamma High	0.75	18.40	0.02	0.12	0.07	0.25	1.61	0.80
Gamma Low	0.89	15.38	0.03	0.25	0.09	0.10	1.80	0.98
Shift Intensity	1.00	∞	0.00	0.00	0.00	0.00	2.00	1.00
Translation	0.65	18.28	0.02	0.12	0.06	0.36	1.07	0.53
Elastic Deform	0.87	27.56	0.00	0.01	0.01	0.06	1.32	0.95

For all applied distortions, all reference metric scores monotonously measure lower similarity for increasing distortion strengths.

Without applying any normalization, all metrics beside NMI are very sensitive to intensity shifts (see Tab. 5). However, with any normalization method, intensity shifts are fully compensated, and all metrics measure perfect similarity.

Across all normalization methods, all metrics are very sensitive to translation and not very sensitive to replace artifacts.

SSIM similarity scores for strong blurring are very high, compared to most other distortions.

Gaussian noise is better detected with Minmax normalization, while stripe artifacts seem to be less detected with Zscore normalization.

PSNR scores generally display only very small changes for strengths larger than 2 (see Fig. A.1). PSNR values are higher for Zscore normalization.

Images distorted with Gaussian blurring and ghosting artifacts receive very high PSNR similarity scores, especially with small distortion strengths.

Table 7. Metric results with cMinmax normalization (clip at 5%-85%). The darker the background the more sensitive the metric for this distortion.

metric low→high	SSIM 0→1	PSNR 0→∞	MSE 0→∞	NMSE ∞→0	MAE 0→∞	LPIPS 1→0	NMI 1→2	PCC 0→1
Distortions								
Bias Field	0.83	11.95	0.07	0.17	0.12	0.15	1.26	0.80
Ghosting	0.71	27.29	0.00	0.00	0.03	0.05	1.30	0.99
Stripe Artifact	0.14	18.51	0.01	0.04	0.08	0.52	1.36	0.95
Gaussian Blur	0.91	25.99	0.00	0.01	0.02	0.23	1.36	0.99
Gaussian Noise	0.15	14.22	0.04	0.10	0.16	0.81	1.13	0.93
Replace Artifact	0.86	19.38	0.01	0.03	0.03	0.08	1.38	0.96
Gamma High	0.93	19.17	0.01	0.03	0.05	0.07	1.84	0.97
Gamma Low	0.94	22.81	0.01	0.02	0.03	0.07	1.82	0.99
Shift Intensity	1.00	∞	0.00	0.00	0.00	0.00	2.00	1.00
Translation	0.59	8.83	0.13	0.34	0.18	0.41	1.07	0.56
Elastic Deform	0.81	20.00	0.01	0.03	0.03	0.08	1.29	0.97

Table 8. Metric results with Zscore normalization. The darker the background the more sensitive the metric to this distortion.

metric low→high	SSIM 0→1	PSNR 0→∞	MSE 0→∞	NMSE ∞→0	MAE 0→∞	LPIPS 1→0	NMI 1→2	PCC 0→1
Distortions								
Bias Field	0.80	24.62	0.46	0.46	0.42	0.15	1.28	0.77
Ghosting	0.97	37.85	0.01	0.01	0.08	0.09	1.37	0.99
Stripe Artifact	0.54	28.85	0.09	0.09	0.23	0.53	1.36	0.96
Gaussian Blur	0.94	33.98	0.03	0.03	0.07	0.25	1.41	0.99
Gaussian Noise	0.45	28.03	0.14	0.14	0.30	0.82	1.16	0.93
Replace Artifact	0.89	27.73	0.12	0.12	0.11	0.09	1.40	0.94
Gamma High	0.85	35.05	0.41	0.41	0.36	0.18	1.61	0.80
Gamma Low	0.95	32.29	0.04	0.04	0.10	0.09	1.80	0.98
Shift Intensity	1.00	∞	0.00	0.00	0.00	0.00	2.00	1.00
Translation	0.58	18.28	0.93	0.93	0.49	0.44	1.07	0.53
Elastic Deform	0.87	28.09	0.11	0.11	0.10	0.09	1.32	0.95

Table 9. Non-reference metric results without normalization (Left) and with cMinMax normalization with clipping at 5% (Right). The darker the background the more sensitive the metric to this distortion.

metric low→high	BLUR	MNG	MSN	metric low→high	BLUR	MNG	MSN
Bias Field	0.37	0.15	0.97	Bias Field	0.39	0.16	0.97
Ghosting	0.34	0.19	0.84	Ghosting	0.36	0.27	0.85
Stripe Artifact	0.20	0.37	0.32	Stripe Artifact	0.20	0.37	0.32
Gaussian Blur	0.52	0.21	0.99	Gaussian Blur	0.52	0.21	0.99
Gaussian Noise	0.18	0.14	0.52	Gaussian Noise	0.18	0.14	0.53
Replace Artifact	0.33	0.17	0.97	Replace Artifact	0.35	0.17	0.97
Gamma High	0.27	0.12	0.92	Gamma High	0.32	0.15	0.95
Gamma Low	0.35	0.17	0.97	Gamma Low	0.35	0.17	0.98
Shift Intensity	0.33	0.16	0.96	Shift Intensity	0.35	0.17	0.97
Translation	0.33	0.16	0.97	Translation	0.35	0.17	0.97
Elastic Deform	0.36	0.18	0.97	Elastic Deform	0.37	0.19	0.98
Reference	0.33	0.16	0.96	Reference	0.35	0.17	0.97

All error metrics (MSE, MAE and NMSE) strongly vary in their value range, depending on the normalization method. They are consistently most sensitive to translation and then to bias field, and gamma transforms. As cMinMax partially compensates the effect of the gamma transforms, the error metrics hardly find dissimilarities in the gamma transformed images with this normalization.

The segmentation scores (see Tab. 5, and Fig. A.4) for all three classes are very similar. Intensity shift has no effect due to preprocessing with z-score normalization. The effect of elastic deforms and ghosting artifacts on the segmentation are very limited. Gaussian noise and stripe artifacts most strongly impair segmentation. Translated segmentations have decreasing overlap and thereby very low DICE scores.

4.2 Non-Reference Metrics

The results for all strengths are given in Fig. A.5. For the maximum strength (s=5), the results are summarized in Tab. 9 without normalization and for cMinMax normalization.

Minmax normalization and Zscore normalization do not have any effect on the selected non-reference metrics, therefore these results are not shown here.

For the BLUR metric, scores clearly increase for blurred images, but also clearly decrease compared to the reference for stripe artifacts, Gaussian noise and the gamma transform for $\gamma > 1$. For small strengths of translation and elastic deformation slightly increased blurriness is measured, but drops again for strengths > 3 .

Compared to the reference images, MNG strongly drops for images with stripe artifacts. With cMinMax normalization, MNG also detects ghosting.

MSN decreased most strongly for stripe artifacts, Gaussian noise and ghosting. The difference for higher distortion strengths is only small, while the lowest distortions are already detected.

5 Adverse Examples

In the following, special characteristics of the analyzed metrics, which can be derived from their definition or the experimental results above, are show-cased. We present adverse examples (see Fig. 2-6), where similarity metrics do not perform as intended or expected.

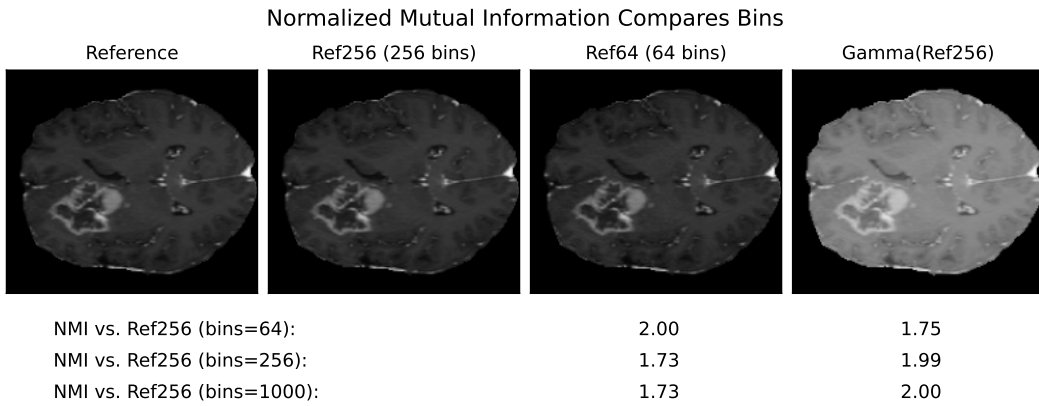


Figure 2. For calculation of NMI, images need to be discretized to histograms. The number and distance of bins chosen to compare an image with its reference has large influence to the resulting NMI score. An image reduce to 6-bit (64 bins) already decreases the NMI score, calculated with 256 bins (8-bit) to 1.73, although the difference is hardly visible. If NMI also uses only 64 bins, a perfect NMI score of 2.0 is obtained. At the same time, a gamma transformed image can achieve a perfect NMI score, if the intensities of one bin in the reference image are mapped into a unique bin in the transformed images as well. With 1000 bins used for NMI calculation, all intensities of one bin in the reference image end up in one and the same separate bin in the gamma transformed image. The strong visual difference in contrast in the gamma transformed image is not captured by NMI.

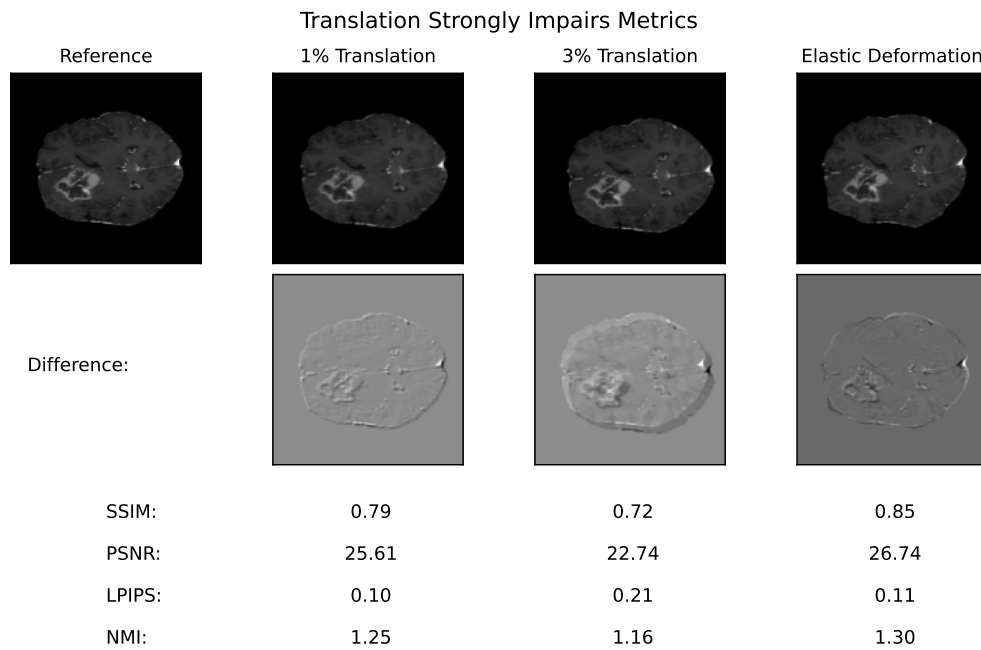


Figure 3. Metric assessed similarity strongly decreases, when images to be compared are only slightly misaligned. For translation of all pixels, the decrease is stronger than for elastic deformation, which effects a smaller set of pixels. Misalignment can be a problem for confirming high similarity between synthesized and target images.

Blurring Improves SSIM of Distorted Images

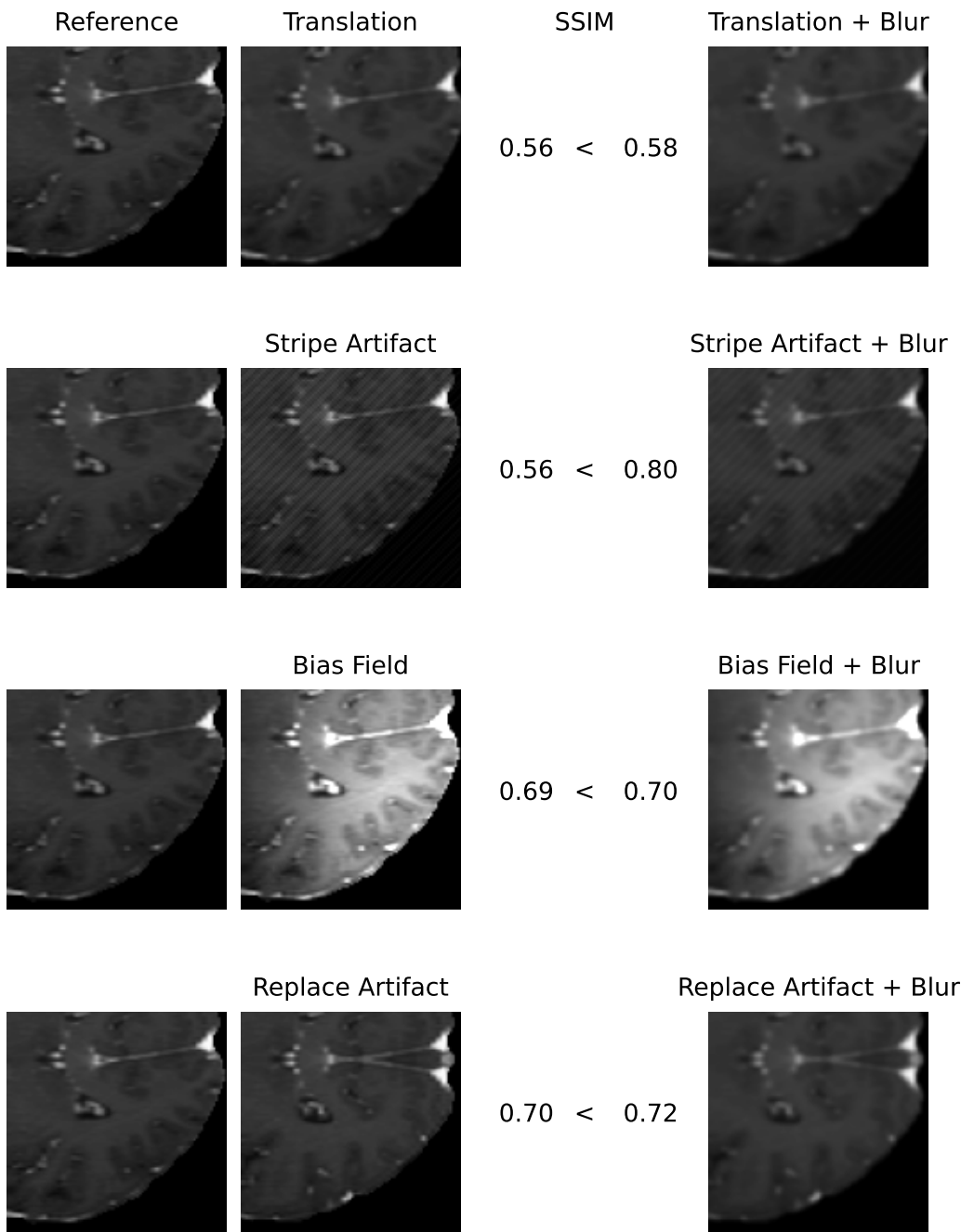


Figure 4. Images, distorted by translation, stripe artifacts, bias field or replace artifacts, show larger similarity to the reference, when they are additionally blurred. Partially, this might be expected, because distortions are weakened by blurring. But in image synthesis trained with SSIM, this may lead to blurry results.

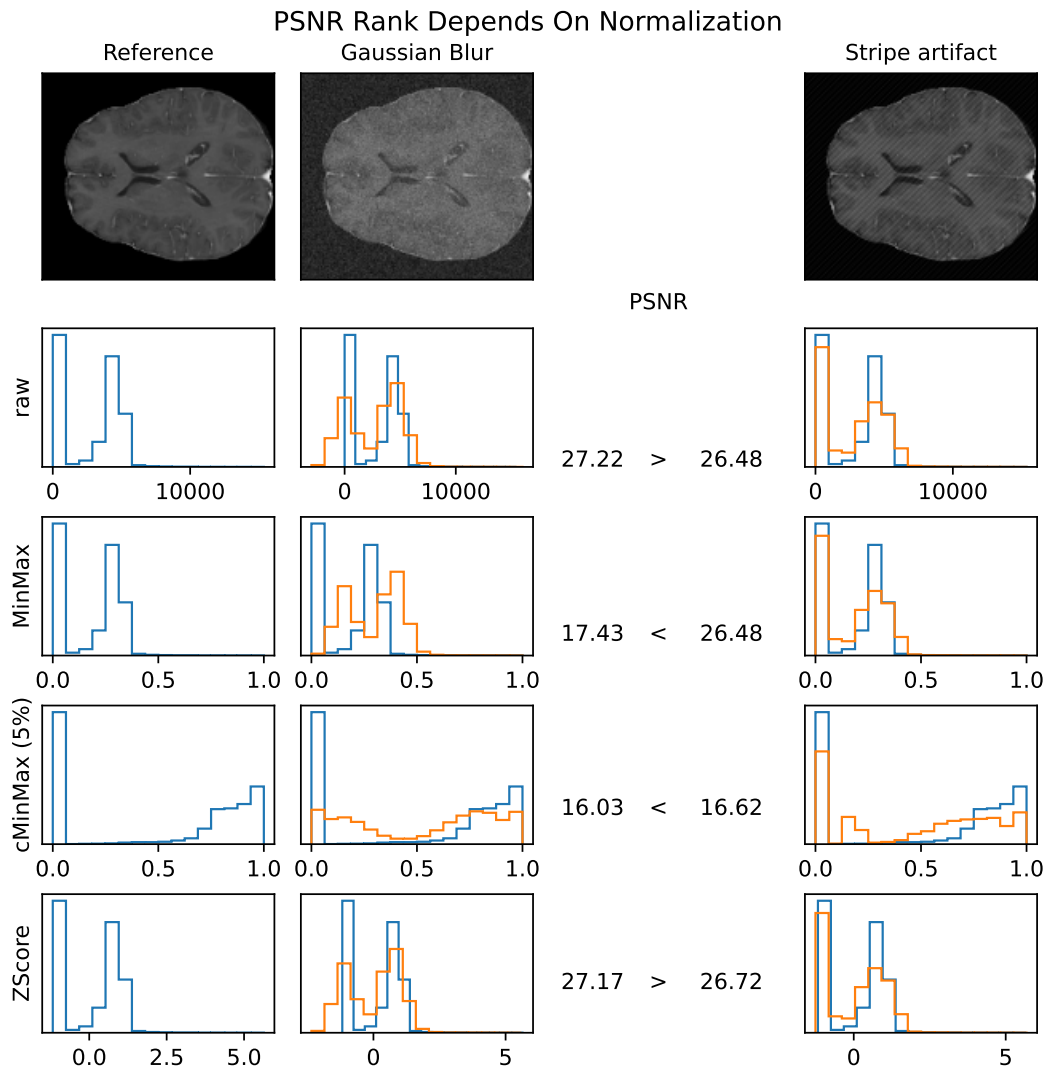


Figure 5. PSNR scores strongly depend on the normalization method. After normalization of images with Gaussian blur or stripe artifacts with different methods very different PSNR values are obtained. When comparing two images to the same reference, the PSNR values may even rank the images differently, depending on the normalization method. Therefore, PSNR values and rankings cannot be compared between studies, when the exact normalization methods is not reported.

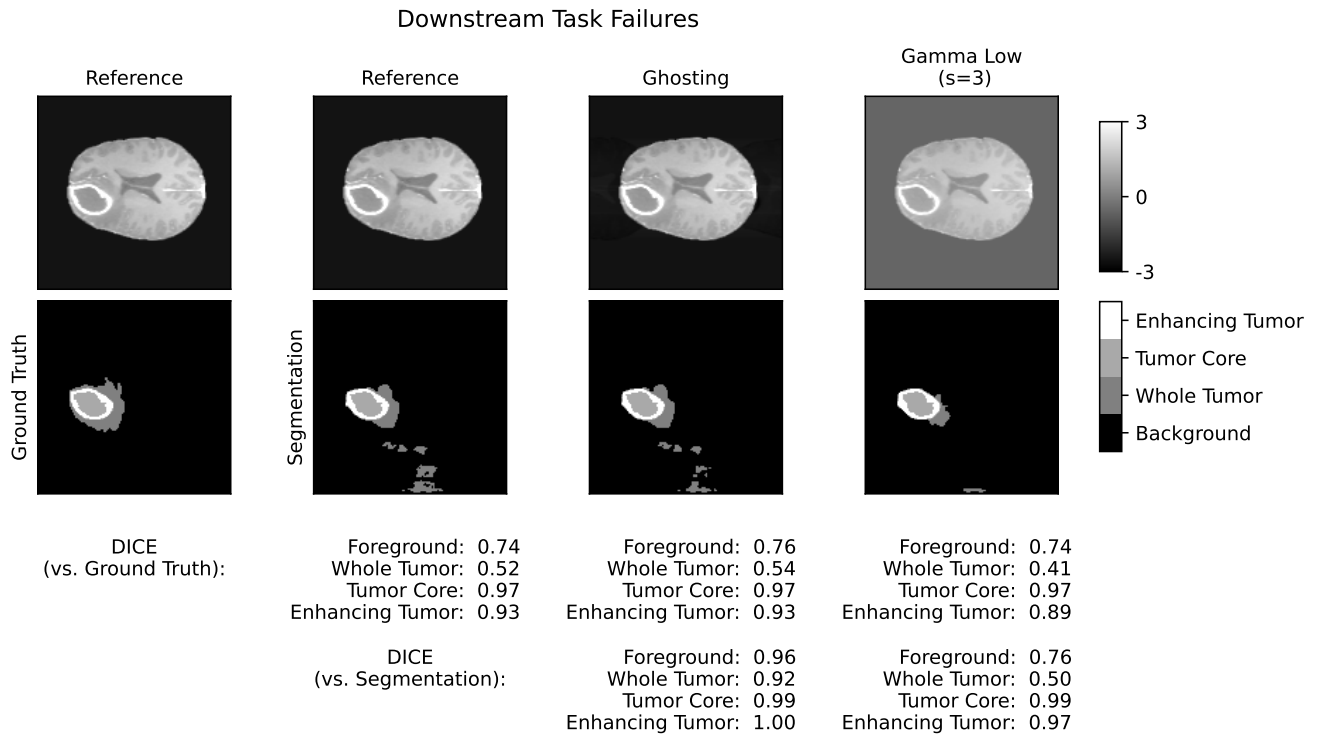


Figure 6. The evaluation with a downstream task is limited to the performance of the downstream task. In this example a large fraction of background is segmented as "whole tumor". The segmentation model was trained on smaller crops with less background and without background artifacts. Although the segmentation of the gamma transformed image seems to better fit the ground truth in the true tumor region, the dice score is noticeably lower, than for the segmentation of the image with ghosting, which displays very similar background artifacts as the reference segmentation. A different segmentation model, or a human could have segmented the tumor nearly equally well as in the reference image by simply ignoring the background. The dice scores between distorted and reference image segmentations do not correlate well with the similarity between distorted and reference image in the tumor region.

6 Discussion

The experiments and adverse examples demonstrate specific strengths and weaknesses of the analyzed metrics. Although SSIM and PSNR are frequently used for the evaluation of synthetic MR images, they are strongly decreased by constant intensity shifts if no normalization is applied. PSNR is very dependent on the kind of normalization, which complicates its use as a comprehensive metric for comparing studies of different authors. SSIM underestimates blurring and thereby favors blurred or additionally blurred images over other distortions.

As all other analyzed metrics, SSIM and PSNR are both very sensitive to translation, which is rather be caused by misaligned target images, than by dissimilarity of synthesized images. When paired input and target images are not acquired by the same hardware or not immediately at the same time points, special care must be taken, to ensure spatial alignment of input and target images.

Some of these observations have already been mentioned by other authors. Similar to SSIM, MSE and MAE were reported to create blurry images⁶². And PSNR and MSE were mentioned to be sensitive to the normalization method³³.

Replace artifacts remain underestimated by most similarity metrics. For those artifacts, that resemble structures of diagnostic interest, the evaluation of segmentations with a specific segmentation model is useful. In our evaluation, we use a segmentation model, that was trained to detect different tumor regions. It successfully detects replace artifacts, where the tumor is doubled or removed.

The non-reference metrics can give valuably additional information about the quality of synthesized images. Blurring is easily and reliably detected by the BLUR metric. However, assessed blurriness decreases with other distortions, such as Gaussian noise, stripe artifacts or gamma transforms, when these increase image contrast.

The MSN metrics represents the line-wise correlation between neighboring lines. The reference value in our experiments lies at 96%, which is probably caused by high anatomical consistency in the present pixel spacing. It strongly decreases for stripe artifacts, which fits to the fact, that the stripes change relations between local image intensities and are not oriented along the x- or y-axis. Random Gaussian noise, reduces statistical correlation and thereby also MSN. Ghosting also reduces MSN, as it additionally distorts image intensities locally.

The MNG metric only slightly increases with ghosting. One reason could be the relative weak scaling of the ghost intensity in our experiments. In contrast, stripe artifacts significantly increased the MNG metrics. Compared to MSN, by coincidence, stripes seem to be in the same phase at the half-image width distance and thereby drastically increase line-wise correlation.

In comparison to other studies, we do not compare the metric scores to human quality assessment. For each type of distortion, we tried to select five comparable strengths. The reader may decide by view of Tabs. 3 and 4, if lowest and highest strengths seem properly scaled. Even though some strengths would be chosen differently by others, the overall qualitative observations about which metrics are most sensitive towards which kind of distortions and the following conclusions would be similar.

7 Conclusions

For the validation of medical image-to-image translation, we gave a broad overview of possible metrics and for nine reference and three non-reference metrics a detailed study of their sensitivity to MR specific distortions.

As a conclusion, we give a few recommendations for the selection and application of appropriate validation metrics.

- As reference metrics the combination of SSIM, LPIPS, MSE and NMI is able to detect a large set of undesired distortions. PCC, NMSE and MAE do not give much additional information. MSE is more frequently used and therefore best suited for comparison to previous studies. The use of PSNR is not recommended.
- As non-reference quality metrics, BLUR reliably detects blurry images, which might not be detected by SSIM or MSE. MSN can detect artifacts that reduce anatomical consistency and also detect distortions, that interfere with blurriness assessment by the BLUR metric.
- For SSIM, LPIPS and MSE we recommend z-score normalization. NMI should be used without normalization. The normalization method must be reported in detail with all parameter whenever metric scores are reported. Normalization must be considered, when comparing scores across studies. The data range parameter L of SSIM should be set to the actual intensity range and must be reported as part of the normalization method.
- If input images and target images are not spatially aligned, they must be registered with highest possible precision before evaluating with reference metrics.
- A segmentation downstream task is useful for evaluation, because image synthesis models are able to synthesize artificial structures relevant for possible downstream tasks. The segmentation model should therefore be able to segment task

specific structures of interest and can be trained with desired or inconsequential distortions. The performance of the segmentation model must be verified before using the segmentations for similarity assessment.

In summary, the metrics for evaluation of image-to-image MR synthesis models must be selected carefully. Frequently used SSIM and PSNR cover a large range of distortions, but have specific weaknesses, that must be covered by other metrics. Specifically PSNR does not seem appropriate for image synthesis evaluation. We highlight some adverse examples, where metrics do not provide the expected or desired values and suggest many other metrics in addition to SSIM, that are able to detect MR specific and typical distortions.

For the selection of metrics and normalization methods, the set of admitted and undesired distortions should be considered. Which metrics are most appropriate for which kind of distortions can be directly derived from our experimental results.

As metrics are also often used as loss functions for model training⁵⁴, the selection of appropriate metrics as loss functions or validation metrics can directly improve image synthesis models before evaluation and speed up model development.

References

1. Saharia, C. *et al.* Palette: Image-to-image diffusion models. In *ACM SIGGRAPH 2022 Conference Proceedings*, SIGGRAPH '22, DOI: [10.1145/3528233.3530757](https://doi.org/10.1145/3528233.3530757) (Association for Computing Machinery, New York, NY, USA, 2022).
2. Isola, P., Zhu, J.-Y., Zhou, T. & Efros, A. A. Image-to-image translation with conditional adversarial networks. In *2017 IEEE Conference on Computer Vision and Pattern Recognition (CVPR)*, 5967–5976, DOI: [10.1109/CVPR.2017.632](https://doi.org/10.1109/CVPR.2017.632) (2017).
3. Goodfellow, I. *et al.* Generative adversarial nets. In Ghahramani, Z., Welling, M., Cortes, C., Lawrence, N. & Weinberger, K. (eds.) *Advances in Neural Information Processing Systems*, vol. 27 (Curran Associates, Inc., 2014).
4. Rezende, D. & Mohamed, S. Variational inference with normalizing flows. In Bach, F. & Blei, D. (eds.) *Proceedings of the 32nd International Conference on Machine Learning*, vol. 37 of *Proceedings of Machine Learning Research*, 1530–1538 (PMLR, Lille, France, 2015).
5. Kingma, D. P. & Welling, M. Auto-encoding variational bayes. In *International Conference on Learning Representations* (2014).
6. Ho, J., Jain, A. & Abbeel, P. Denoising diffusion probabilistic models. In Larochelle, H., Ranzato, M., Hadsell, R., Balcan, M. & Lin, H. (eds.) *Advances in Neural Information Processing Systems*, vol. 33, 6840–6851 (Curran Associates, Inc., 2020).
7. Kebaili, A., Lapuyade-Lahorgue, J. & Ruan, S. Deep Learning Approaches for Data Augmentation in Medical Imaging: A Review. *J. imaging* **9**, DOI: [10.3390/jimaging9040081](https://doi.org/10.3390/jimaging9040081) (2023). Place: Switzerland.
8. Kaji, S. & Kida, S. Overview of image-to-image translation by use of deep neural networks: denoising, super-resolution, modality conversion, and reconstruction in medical imaging. *Radiol. Phys. Technol.* **12**, 235–248 (2019).
9. Weigert, M. *et al.* Content-aware image restoration: pushing the limits of fluorescence microscopy. *Nat. Methods* **15**, 1090 – 1097 (2018).
10. Bahrami, A., Karimian, A. & Arabi, H. Comparison of different deep learning architectures for synthetic ct generation from mr images. *Phys. Medica* **90**, 99–107, DOI: <https://doi.org/10.1016/j.ejmp.2021.09.006> (2021).
11. Lu, J., Öfverstedt, J., Lindblad, J. & Sladoje, N. Is image-to-image translation the panacea for multimodal image registration? a comparative study. *PLOS ONE* **17**, 1–33, DOI: [10.1371/journal.pone.0276196](https://doi.org/10.1371/journal.pone.0276196) (2022).
12. Raut, P., Baldini, G., Schöneck, M. & Caldeira, L. Using a generative adversarial network to generate synthetic mri images for multi-class automatic segmentation of brain tumors. *Front. Radiol.* **3**, DOI: [10.3389/fradi.2023.1336902](https://doi.org/10.3389/fradi.2023.1336902) (2024).
13. Mallio, C. A. *et al.* Artificial intelligence to reduce or eliminate the need for gadolinium-based contrast agents in brain and cardiac mri: A literature review. *Investig. Radiol.* **58** (2023).
14. Borji, A. Pros and cons of gan evaluation measures: New developments. *Comput. Vis. Image Underst.* **215**, 103329, DOI: <https://doi.org/10.1016/j.cviu.2021.103329> (2022).
15. Pianykh, O. S., Pospelova, K. & Kamboj, N. H. Modeling human perception of image quality. *J. Digit. Imaging* **31**, 768–775 (2018).
16. Sampat, M. P., Wang, Z., Gupta, S., Bovik, A. C. & Markey, M. K. Complex wavelet structural similarity: A new image similarity index. *IEEE Transactions on Image Process.* **18**, 2385–2401, DOI: [10.1109/TIP.2009.2025923](https://doi.org/10.1109/TIP.2009.2025923) (2009).
17. Li, Y. *et al.* Samscore: A semantic structural similarity metric for image translation evaluation (2023). [2305.15367](https://doi.org/10.4236/ojs.20230315367).

18. Ding, K., Ma, K., Wang, S. & Simoncelli, E. P. Image quality assessment: Unifying structure and texture similarity. *IEEE Transactions on Pattern Analysis Mach. Intell.* **44**, 2567–2581, DOI: [10.1109/TPAMI.2020.3045810](https://doi.org/10.1109/TPAMI.2020.3045810) (2022).
19. Ponomarenko, N. *et al.* A new color image database tid2013: Innovations and results. In Blanc-Talon, J., Kasinski, A., Philips, W., Popescu, D. & Scheunders, P. (eds.) *Advanced Concepts for Intelligent Vision Systems*, 402–413 (Springer International Publishing, Cham, 2013).
20. Sheikh, H., Sabir, M. & Bovik, A. A statistical evaluation of recent full reference image quality assessment algorithms. *IEEE Transactions on Image Process.* **15**, 3440–3451, DOI: [10.1109/TIP.2006.881959](https://doi.org/10.1109/TIP.2006.881959) (2006).
21. Nečasová, T., Burgos, N. & Svoboda, D. Validation and evaluation metrics for medical and biomedical image synthesis. In Burgos, N. & Svoboda, D. (eds.) *Biomedical Image Synthesis and Simulation*, The MICCAI Society Book Series, chap. 25, 573–600 (Academic Press, 2022).
22. Yi, X., Walia, E. & Babyn, P. Generative adversarial network in medical imaging: A review. *Med. Image Analysis* **58**, 101552, DOI: <https://doi.org/10.1016/j.media.2019.101552> (2019).
23. McNaughton, J. *et al.* Machine learning for medical image translation: A systematic review. *Bioengineering* **10** (2023).
24. Haase, R. *et al.* Artificial contrast: Deep learning for reducing gadolinium-based contrast agents in neuroradiology. *Investig. Radiol.* **58**, 539–547 (2023).
25. Mudeng, V., Kim, M. & Choe, S.-w. Prospects of structural similarity index for medical image analysis. *Appl. Sci.* **12** (2022).
26. Huynh-Thu, Q. & Ghanbari, M. Scope of validity of psnr in image/video quality assessment. *Electron. Lett.* **44**, 800–801 (2008).
27. <https://www.fda.gov/medical-devices/software-medical-device-samd/artificial-intelligence-and-machine-learning-aiml-enabled-medical-devices>
28. Reinke at al., A. Understanding metric-related pitfalls in image analysis validation. *Nat. Methods* **21**, 82 – 194 (2024).
29. Maier-Hein et al., L. Metrics reloaded: recommendations for image analysis validation. *Nat. Methods* **21**, 195–212 (2024).
30. Baltruschat, I. M., Janbakhshi, P. & Lenga, M. Brasyn 2023 challenge: Missing mri synthesis and the effect of different learning objectives (2024). [2403.07800](https://doi.org/10.4236/ojs.20240402407800)
31. Goodfellow, I., Bengio, Y. & Courville, A. *Deep Learning*, chap. 12.2.1 Preprocessing, 448 (MIT Press, 2016). <http://www.deeplearningbook.org>.
32. Tellez, D. *et al.* Quantifying the effects of data augmentation and stain color normalization in convolutional neural networks for computational pathology. *Med. Image Analysis* **58**, 101544, DOI: <https://doi.org/10.1016/j.media.2019.101544> (2019).
33. Reinhold, J. C., Dewey, B. E., Carass, A. & Prince, J. L. Evaluating the impact of intensity normalization on MR image synthesis. In Angelini, E. D. & Landman, B. A. (eds.) *Medical Imaging 2019: Image Processing*, vol. 10949, 109493H, DOI: [10.1117/12.2513089](https://doi.org/10.1117/12.2513089). International Society for Optics and Photonics (SPIE, 2019).
34. Ammari, S. *et al.* Can deep learning replace gadolinium in neuro-oncology?: A reader study. *Investig. Radiol.* **57**, 99–107 (2022).
35. Haase, R. *et al.* Reduction of gadolinium-based contrast agents in mri using convolutional neural networks and different input protocols: Limited interchangeability of synthesized sequences with original full-dose images despite excellent quantitative performance. *Investig. Radiol.* **58** (2023).
36. Nyúl, L. G. & Udupa, J. K. On standardizing the mr image intensity scale. *Magn. Reson. Medicine* **42**, 1072–1081 (1999).
37. Shinohara, R. T. *et al.* Statistical normalization techniques for magnetic resonance imaging. *NeuroImage: Clin.* **6**, 9–19 (2014).
38. Onofrey, J. A. *et al.* Generalizable multi-site training and testing of deep neural networks using image normalization. *Proceedings. IEEE Int. Symp. on Biomed. Imaging* 348–351 (2019).
39. Torchmetrics - measuring reproducibility in pytorch, DOI: [10.21105/joss.04101](https://doi.org/10.21105/joss.04101) (2022).
40. van der Walt, S. *et al.* scikit-image: image processing in Python. *PeerJ* **2**, e453, DOI: [10.7717/peerj.453](https://doi.org/10.7717/peerj.453) (2014).
41. Wang, Z., Bovik, A. C., Sheikh, H. R. & Simoncelli, E. P. Image quality assessment: from error visibility to structural similarity. *IEEE Transactions on Image Process.* **13**, 600–12 (2004).
42. Wang, Z., Simoncelli, E. & Bovik, A. Multiscale structural similarity for image quality assessment. In *The Thirty-Seventh Asilomar Conference on Signals, Systems and Computers, 2003*, vol. 2, 1398–1402 Vol.2, DOI: [10.1109/ACSSC.2003.1292216](https://doi.org/10.1109/ACSSC.2003.1292216) (2003).

43. Ding, K. "iqa optimization" (2020).
44. Huynh-Thu, Q. & Ghanbari, M. Scope of validity of psnr in image/video quality assessment. *Electron. Lett.* **44**, 800–801(1) (2008).
45. Pedregosa, F. *et al.* Scikit-learn: Machine learning in Python. *J. Mach. Learn. Res.* **12**, 2825–2830 (2011).
46. "perceptual similarity metric and dataset".
47. Zhang, R., Isola, P., Efros, A. A., Shechtman, E. & Wang, O. The unreasonable effectiveness of deep features as a perceptual metric. *CoRR* **abs/1801.03924** (2018). [1801.03924](https://arxiv.org/abs/1801.03924).
48. Ding, K.
49. McCormick, M., Liu, X., Ibanez, L., Jomier, J. & Marion, C. Itk: enabling reproducible research and open science. *Front. Neuroinformatics* **8**, DOI: [10.3389/fninf.2014.00013](https://doi.org/10.3389/fninf.2014.00013) (2014).
50. Maes, F., Collignon, A., Vandermeulen, D., Marchal, G. & Suetens, P. Multimodality image registration by maximization of mutual information. *IEEE Transactions on Med. Imaging* **16**, 187–198, DOI: [10.1109/42.563664](https://doi.org/10.1109/42.563664) (1997).
51. Crété-Roffet, F., Dolmiere, T., Ladret, P. & Nicolas, M. The Blur Effect: Perception and Estimation with a New No-Reference Perceptual Blur Metric. In *SPIE Electronic Imaging Symposium Conf Human Vision and Electronic Imaging*, vol. XII, EI 6492–16 (San Jose, United States, 2007).
52. Choi, M. G., Jung, J. H. & Jeon, J. W. No-reference image quality assessment using blur and noise. *Int. J. Electr. Comput. Eng.* **3**, 184–188 (2009).
53. Schuppert et al., C. Whole-body magnetic resonance imaging in the large population-based german national cohort study: Predictive capability of automated image quality assessment for protocol repetitions. *Investig. Radiol.* **57** (2022).
54. Ding, K., Ma, K., Wang, S. & Simoncelli, E. P. Comparison of image quality models for optimization of image processing systems. *CoRR* **abs/2005.01338** (2020).
55. Baker, A. H., Pinard, A. & Hammerling, D. M. On a structural similarity index approach for floating-point data. *IEEE Transactions on Vis. Comput. Graph.* 1–13, DOI: [10.1109/TVCG.2023.3332843](https://doi.org/10.1109/TVCG.2023.3332843) (2023).
56. Dice, L. R. Measures of the amount of ecologic association between species. *Ecology* **26**, 297–302, DOI: <https://doi.org/10.2307/1932409> (1945).
57. Jayachandran Preetha, C. *et al.* Deep-learning-based synthesis of post-contrast t1-weighted mri for tumour response assessment in neuro-oncology: a multicentre, retrospective cohort study. *The Lancet Digit. Heal.* **3**, e784–e794, DOI: [https://doi.org/10.1016/S2589-7500\(21\)00205-3](https://doi.org/10.1016/S2589-7500(21)00205-3) (2021).
58. Müller-Franzes, G. *et al.* A multimodal comparison of latent denoising diffusion probabilistic models and generative adversarial networks for medical image synthesis. *Sci. Reports* **13**, 12098 (2023).
59. Li, H. B. & et al. The brain tumor segmentation (brats) challenge 2023: Brain mr image synthesis for tumor segmentation bratsyn. *arxiv* (2023).
60. Consortium, M. Monai: Medical open network for ai (2023). <https://docs.monai.io/en/stable/auto3dseg.html>.
61. Cohen, J. P., Luck, M. & Honari, S. Distribution matching losses can hallucinate features in medical image translation. In Frangi, A. F., Schnabel, J. A., Davatzikos, C., Alberola-López, C. & Fichtinger, G. (eds.) *Medical Image Computing and Computer Assisted Intervention – MICCAI 2018*, 529–536 (Springer International Publishing, Cham, 2018).
62. Liu, J. *et al.* Dyefreenet: Deep virtual contrast ct synthesis. In Burgos, N., Svoboda, D., Wolterink, J. M. & Zhao, C. (eds.) *Simulation and Synthesis in Medical Imaging*, 80–89 (Springer International Publishing, Cham, 2020).

Appendix

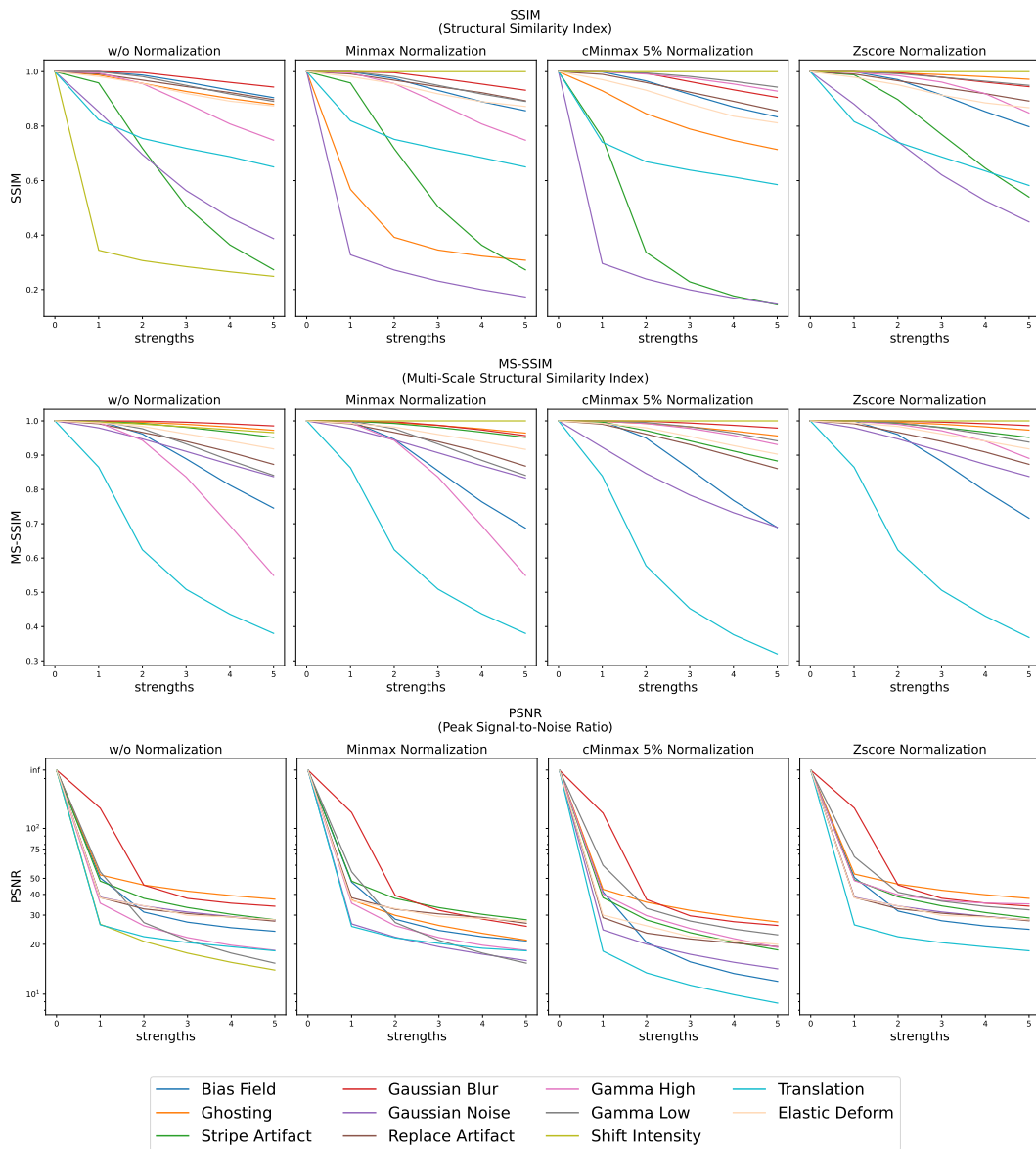


Figure A.1. Evaluation results for SSIM (top), MS-SSIM (middle) and PSNR (bottom) on distorted images.

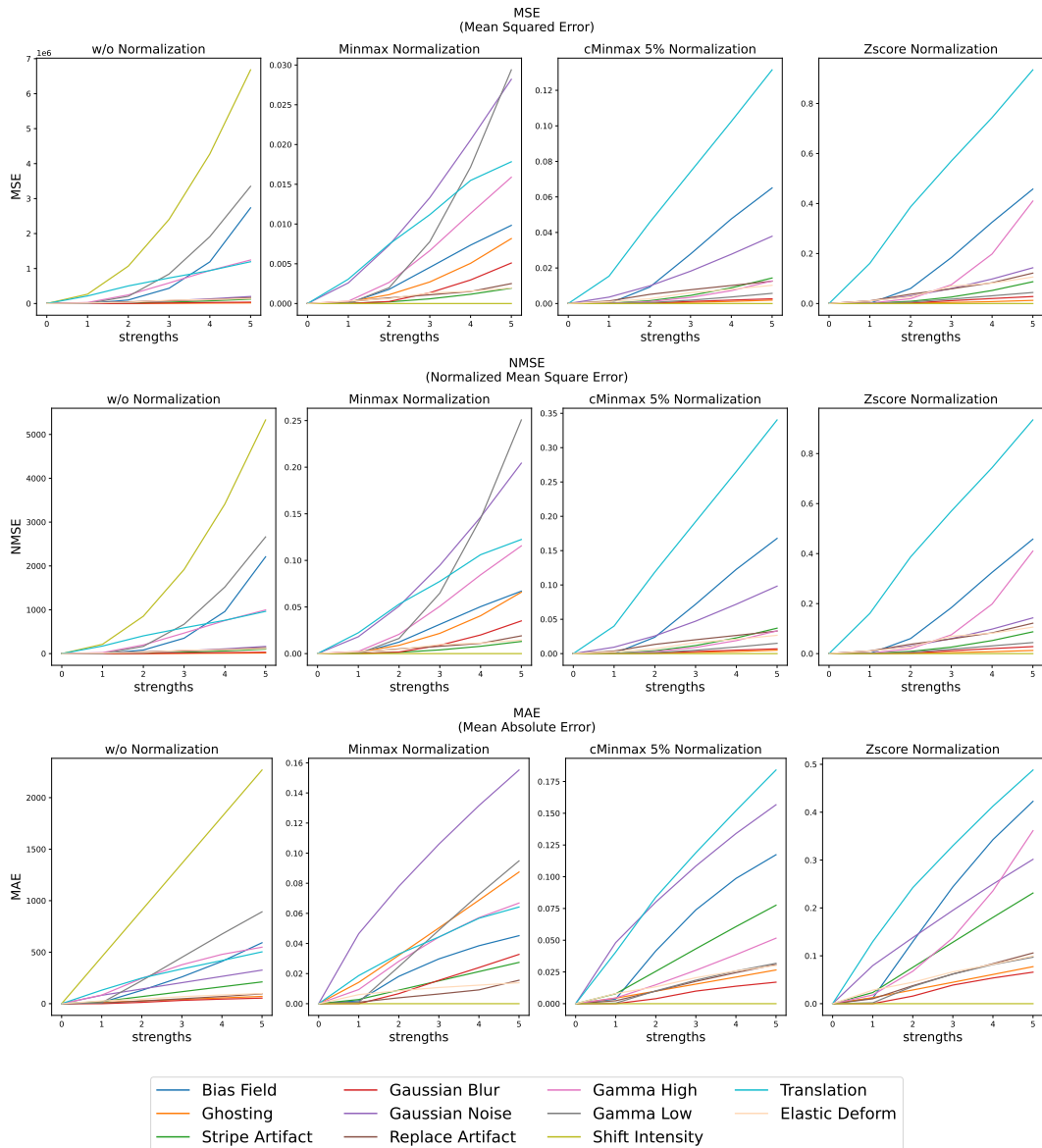


Figure A.2. Evaluation results for MSE (top), NMSE (middle) and MAE (bottom) on distorted images.

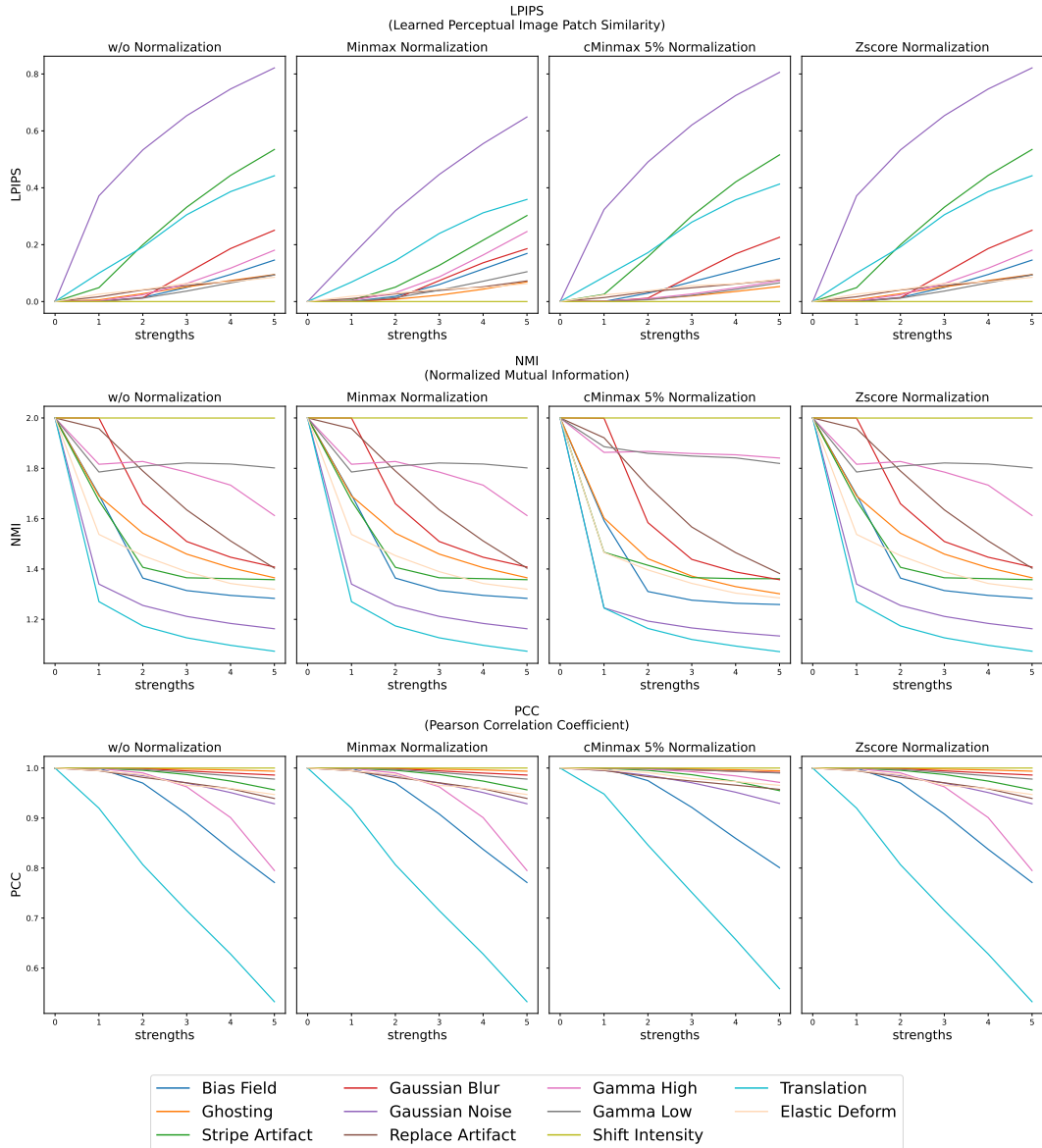


Figure A.3. Evaluation results for LPIPS (top), NMI (middle) and PCC (bottom) on distorted images.

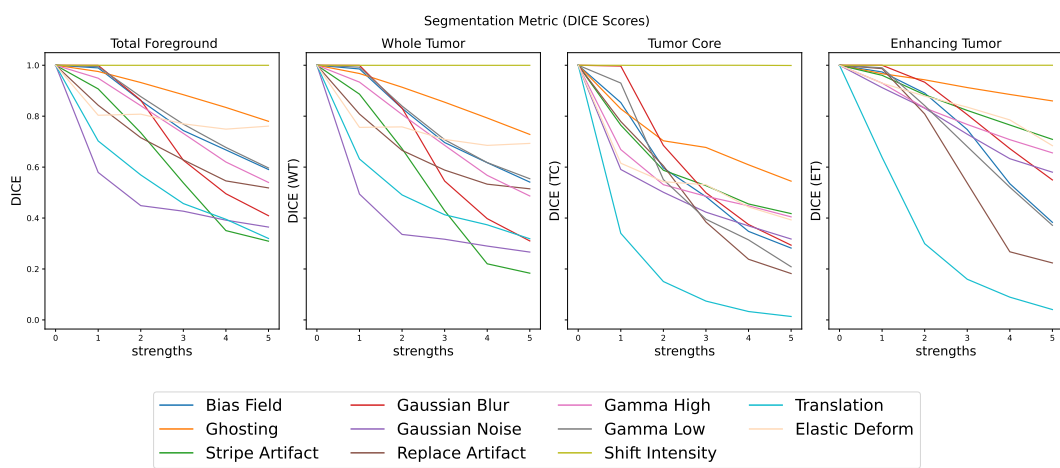


Figure A.4. Evaluation results for segmentation metric

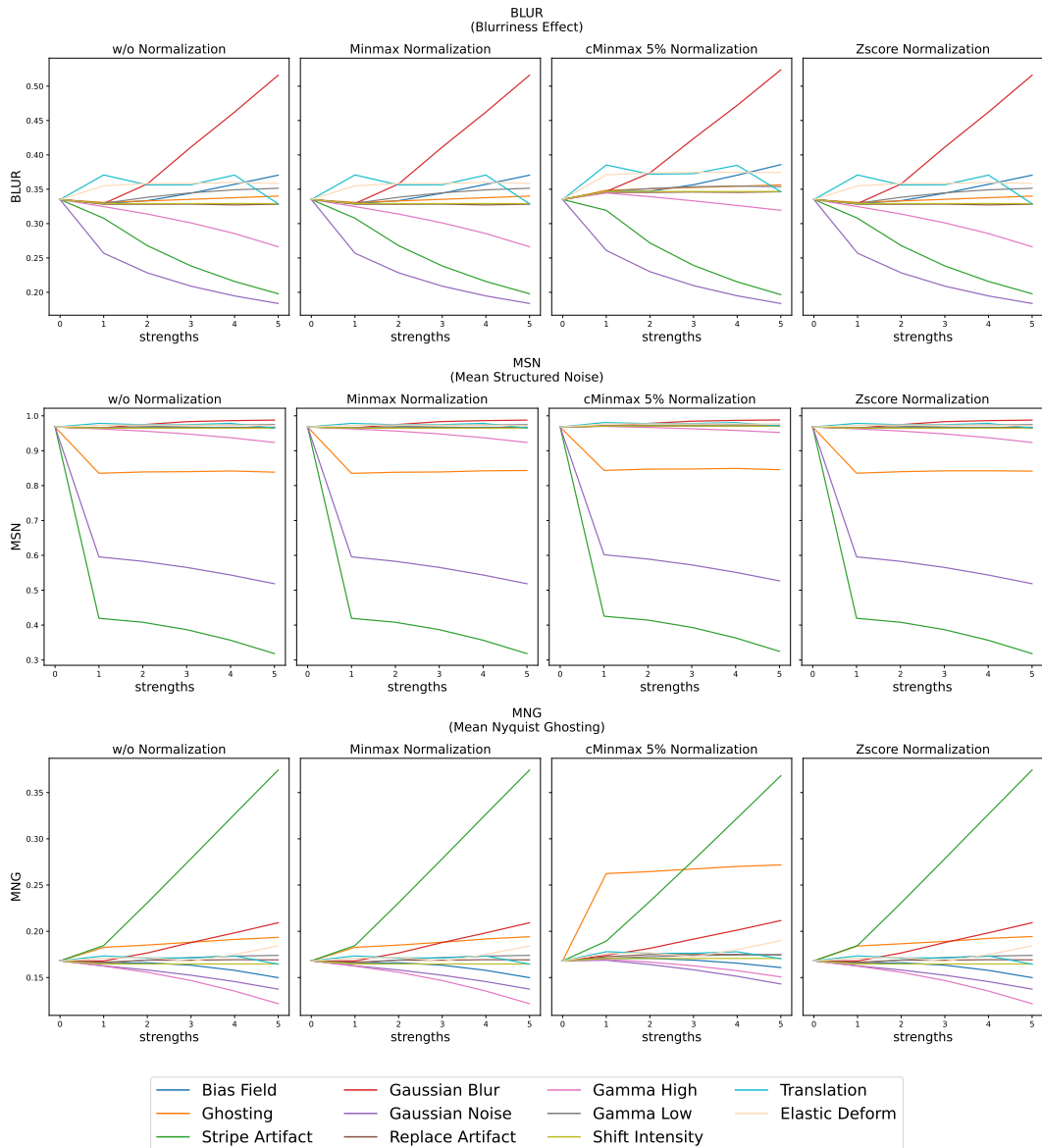


Figure A.5. Evaluation results for non-reference metrics BLUR (top), MSN (middle), MNG (bottom)